MULTIFERROIC BISMUTH FERRITE-LEAD TITANATE AND IRON-GALLIUM CRYSTALLINE SOLUTIONS: STRUCTURE-PROPERTY INVESTIGATIONS

Naigang Wang

Thesis submitted to the Faculty of the Virginia Polytechnic Institute and State University,
in partial fulfillment of the requirements for the degree of
Master of Science
2005
In
Materials Science and Engineering

APPROVED:

Dr. Dwight Viehland, Chair/Advisor
Dr. Jiefang Li
Dr. W. T. Reynolds

May, 17, 2005
Blacksburg, Virginia

Keywords:
Multiferroic; Bismuth ferrite; Iron gallium; Ferroelectricity; Ferromagnetization; Magnetic permeability; Neutron diffraction; Magnetostriction.

MULTIFERROIC BISMUTH FERRITE-LEAD TITANATE AND IRON-GALLIUM CRYSTALLINE SOLUTIONS: STRUCTURE-PROPERTY INVESTIGATIONS

By Naigang Wang
Chair: Dr. Dwight Viehland
Materials Science and Engineering

(ABSTRACT)

Recently, multiferroics-defined as materials with coexistence of at least two of the ferroelectric, ferroelastic and ferromagnetic effects-have attracted enormous research activities. In this thesis, the structure and properties of multiferrioic $BiFeO_3$-x%$PbTiO_3$ and Fe-x%Ga crystalline solutions were investigated.

First, the results show that modified $BiFeO_3$-$PbTiO_3$ based ceramics have significantly enhanced multiferroic properties, relative to $BiFeO_3$ single crystals. The data reveal: (i) a dramatic increase in the induced polarization; and (ii) the establishment of a remnant magnetization by a breaking of the translational invariance of a long-period cycloidal spin structure, via substituent effects. In addition, temperature dependent magnetic permeability investigations of $BiFeO_3$-x$PbTiO_3$ crystalline solutions have shown that aliovalent La substitution results in a significant increase in the permeability.

Second, room temperature high-resolution neutron and x-ray diffraction studies have been performed on Fe-x%Ga crystals for $12<x<25$at%. It has been observed that the structures of both Fe-12%Ga and Fe-25%Ga are tetragonal; however, near the phase boundary between them, an averaged-cubic structure was identified. In addition, an unusual splitting along the transverse direction indicates that the crystals are structurally inhomogeneous.

ACKNOWLEDGEMENTS

I would like to express my sincere gratitude to my advisor Dr. Dwight Viehland. It was his guidance and support that helped me through all the difficult time. I will surely benefit from his creative thoughts, suggestions and dedication throughout the rest of my life. The same gratitude goes to Dr. Jiefang Li and Dr. Dong for their kindly help and support on my research and my life during the past three years.

I also wish to thank my committee member Dr. W. T. Reynolds for his valuable discussions and suggestions in this undertaking.

I would like to thank Dr. J. Chen and Dr. L. E. Cross at PSU for the collaborations on the studied on $BiFeO_3$ based ceramics;

I would like to thank Dr. T. Lograsso at Ames Lab for providing the Fe-Ga samples and for his useful discussions.

I would like to thank Dr P. Gehring at NIST and F. Bai for helping me on the neutron diffraction experiments.

I would like to thank Dr. G. Yee and Dr. G. Wang for teaching me using the SQUID magnetometer.

I would also like to acknowledge the office and technical staff at the MSE department without whom none of this would have been possible.

All the friends and collaborators at Virginia Tech, Hu Cao, Feiming Bai, Li Yan, Junyi Zhai, Zengping Xing and at PSU, Junling Wang, thank you. It is your friendships that make my life here more fun.

I dedicate this thesis to my parents, my wife and my brother.

TABLE OF CONTENT

LIST OF TABLES

LIST OF FIGURES

CHAPTER 1 BACKGROUND

1.1 Primary ferroics

A primary ferroic material exhibits a spontaneous magnetization, a spontaneous polarization or a spontaneous stain. And these spontaneous orders can be reoriented by an external magnetic field, electric field, or mechanical stress below a characteristic temperature (Currie temperature). Table I lists the three simple primary ferroics: ferromagnetic, ferroelectric, and ferroelastic [1].

Table I The three simple primary ferroics

Ferroic class	Orientation states	Switching force	Example
Ferroelectric	Spontaneous polarization (P)	Electric field (E)	$BaTiO_3$
Ferroelastic	Spontaneous strain (S)	Mechanical stress (T)	$Au_xCu_{1-x}Zn$
Ferromagnetic	Spontaneous magnetization (M)	Magnetic field (H)	Fe_3O_4

Basically, ferroics could be characterized by a hysteresis response in the external field, as shown in Figure 1.1. Important parameters such as coercive field, remnant and saturation spontaneous orders are indicated in the figure. Ferroic materials are associated with multi-scale phenomena from atomic/nano scale (atomic/ionic displacement, spin, etc.), mesoscopic scale (domain), to macroscopic scale (strain, electric effects, magnetic effects). Accordingly, they have significant scientific interest and profound technological importance.

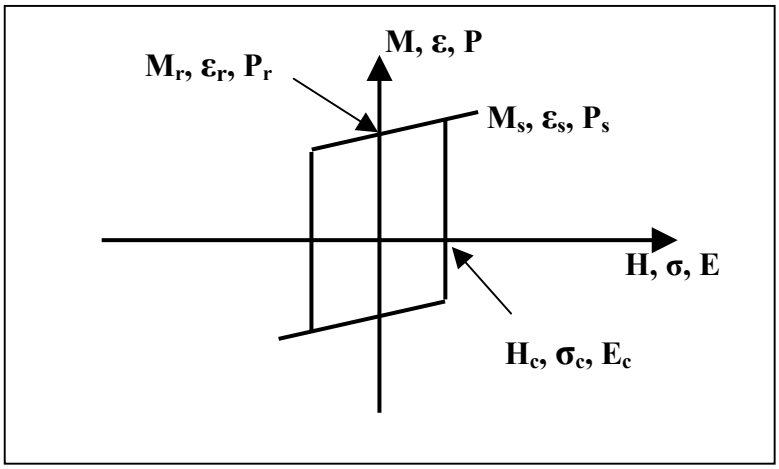

Figure 1.1 Schematic of a hysteresis loop showing the coercive field, remnant and saturation strain, polarization and magnetization.

A domain is a region of the crystal where the order parameter is aligned in a common orientational variation. Prior to application of a field (E, H, σ), the domains are randomly oriented. Thus, no net order parameter exists across the sample. As field is applied and increased, the domains aligned with the fields tend to grow in size; whereas the ones perpendicular to fields decrease in size. This results in the development of a net order parameter. At higher fields, the order parameter response saturates (P_s, H_s, ε_s). Then, if the field is reduced to zero, the domains that were aligned with it will not disappear. Rather a remnant order parameter (P_r, H_r, ε_r) is sustained, and the P-E/M-H/ε-σ response is hysteretic. However, when the field is reversed the domains will switch between equivalent orientational variants. At a critical field, the domain variants have equal population, and the net order parameter is zero. At higher reverse fields, a net order parameter will develop, but in the opposite direction.

1.1.1 Ferroelectric materials

Ferroelectricity (FE) was first discovered in Rochelle salt in 1921. At that time, it was called Seignette-electricity, honoring its discoverer. For the past few decades, ferroelectric materials have received a great amount of interests because of their various uses in many applications such as nonvolatile ferroelectric random access memories (NVFRAM), dynamic random access memories, sensors and microactuators. [2]

A crystal is said to be ferroelectric when it possesses at least two equilibrium orientations of the spontaneous polarization vector in the absence of an external electric field, and the spontaneous polarization can be switched between those orientations by an

electric field. The polar character of the orientation states should represent an absolutely stable configuration in a null field. [3].

Among the thirty-two crystal classes, eleven of them are characterized by the existence of a center of symmetry. The remaining twenty-one crystal classes do not have a center of symmetry. Thus, it is possible for the 21 groups to (i) have one or more polar axes, and (ii) possess odd-rank tensor properties. The only exception is the group 432, which lacks a center of symmetry, but has other symmetry operations that destroy polarity. All non-centrosymmetric point groups exhibit piezoelectric effect that is defined by a change in electric polarity under applied stress, and vice versa. Out of the twenty piezoelectric classes, ten possess a unique polar axis, the spontaneous polarization of which depends on temperature. This is called the pyroelectric effect. Ferroelectric crystals belong to the pyroelectric family, which in addition has a spontaneous polarization can be reversed by external electric field, i.e. more than one equivalent direction for Ps [4].

Among all ferroelectric materials, the most extensively studied and widely used are the perovskite. A perfect perovskite structure has a general formula of ABO_3, where A represents a divalent or trivalent cation, and B is typically a tetravalent or trivalent cation. The origin of ferroelectricity in this family of materials can be explained using the well-known example of barium titanate ($BaTiO_3$). As shown in Figure 1.2, the Ba^{2+} cations are located at the corners of the unit cell. A dipole moment occurs due to relative displacements of the Ti^{4+} and O^{2-} ions from their symmetrical positions.

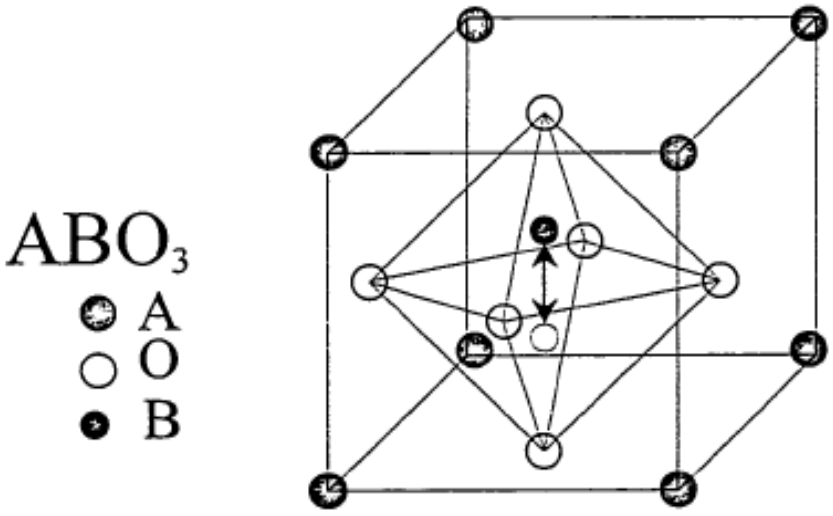

Figure 1.2 Schematic illustration of the unit cell of perovskite ferroelectric materials. Figure adapted from Li. [5]

1.1.2 Ferro-, antiferro-, and ferri-magnetic materials

The phenomenon of magnetism has been known to mankind for many thousands of years. Lodestone (Fe_3O_4) was the first permanent magnetic material to be identified and studied. The magnetic moment of an atom/ion has three principal sources: (1) the spin of electrons; (2) electron orbital angular momentum about the nucleus; and (3) a change in the orbital moment induced by an applied magnetic field. The first two effects give paramagnetic contributions to the magnetization, and the third gives a diamagnetic contribution [6].

In a crystal, the overall magnetic property depends on two factors: (i) the magnetic response associated with each atom/ion, and (ii) the interactions between these magnetic moments. In the case that there are no unpaired electrons around each atom/ion, there will be no net magnetic moments associated with them (bearing in mind that both orbital moments and electron spins cancel to zero in a fully filled orbital), the material will show diamagnetic behavior. When there are unpaired electrons, every atom/ion has a net magnetic moment. Depending on the interactions between the magnetic dipoles, the material may show (i) paramagnetism (PM); (ii) ferromagnetism (FM); (iii) antiferromagnetism (AFM) and (iv) ferrimagnetism (FIM). In a paramagnetic material, alignment of adjacent moments is not observed due to thermal fluctuation. Ferromagnetism consists of parallel aligned adjacent moments. Antiferromagnetic order consists of antiparallel aligned equal moments. And, ferrimagnetic order consists of antiparallel unequal moments, resulting in a non-zero net magnetization.

Ferromagnetism is a very strong magnetic response compared with paramagnetic

and diamagnetic behaviors. It is characterized by a transition temperature (Neel temperature, T_N). Above this temperature, the material is paramagnetic. Below this temperature, it is ferromagnetic.

The magnetic susceptibility, $\chi = \frac{M}{H}$, which defines the degree of magnetization of a material in response to a magnetic field, is a good indication of their magnetic properties. If χ is positive the material is paramagnetic, and the magnetic field is strengthened by the presence of the material. If χ is negative then the material is diamagnetic and the magnetic field is weakened in the presence of the material. The magnetic susceptibility of a ferromagnetic substance is not linear.

1.1.3 Ferroelastic material

Ferroelastic materials develop a spontaneous strain below a phase transition temperature. From the symmetry point of view, the material undergo a structural phase transition from a high symmetry phase to a low symmetry phase, which is characterized by a 'broken symmetry' of the high symmetry phase [7].

The phase transition mechanism results in a spontaneous strain. The spontaneous strain can be quite large. For example, the spontaneous strain of a typical ferroelastic material is >2%. The correlated changes in the enthalpy of the crystal related to this formation of spontaneous strain often reach some 6 KJ/mole, an energy which would reactive equivalent changes in thermochemical phase diagrams of some hundreds of degrees in temperature. In order to release the energy created by the phase transition, a

twin domain structure is often created within a ferroelastic crystal, where the dominant twin planes are oriented approximately perpendicular to each other.

A wall between two adjacent domains can be envisaged as an internal surface of the crystal. The orientation of an individual twin wall is then determined by the condition that the crystal in the low-symmetry phase tends to maintain the total symmetry of the high-symmetry phase as an average. The domains are related equivalent to each other via the symmetry element lost at the phase transition that give rise to the long-range ordered state. It is commonly accepted that stress induced domain wall motion in ferroelastic materials yield hysteretic macroscopic behavior. Mueller et al. [8] showed that nonlinear effects in ferroelastic crystals are related to the properties of ferroelastic domain walls pinned on defects, which became de-pined above a critical stress level. Additionally, Jian and Wayman [9] observed domain wall motion in single-crystal and polycrystalline LaNbO4 ferroelastics under stress, and argued that the nonlinear elastic behavior is a direct result of domain wall motion, rather than the intrinsic properties of the crystal. In addition, Newnham [10] concluded that stress-induced movement of domain walls is the principle source of hysteresis in ferroelastics. A complete analysis of twin structure and domain wall can be seen in reference [8].

Fig. 1. 3 illustrates the stress-induced twin movement of a ferroelasteic $Pb_3(Pb_4)_2$ crystal [8].

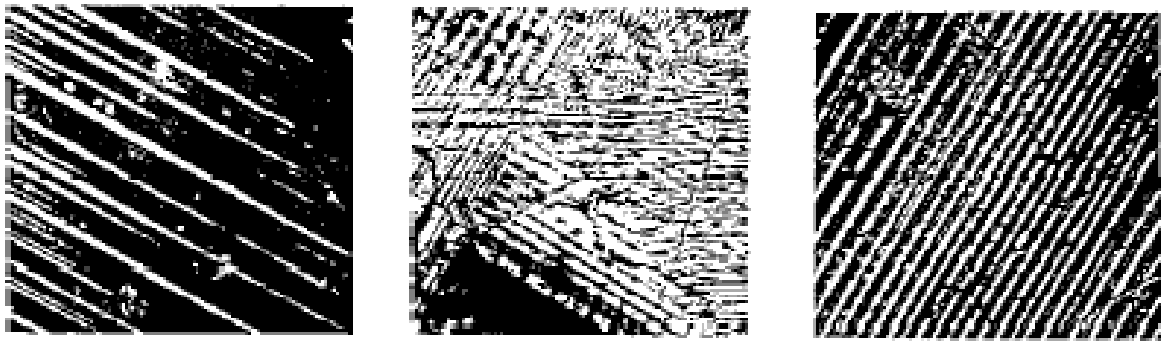

Figure 1.3 Experimentally observed microstructures of lead phosphate. The two fully 'switched' crystals (a) and (c) display striped twin patterns whereas the crystal in the intermediate state (b) shows superposition of various twin orientations.

1.2 Multiferroic materials

Multiferroic materials are single-component materials or composites exhibiting two or more ferroic features such as ferromagnetism, ferroelectricity, or ferroelasticity effects. In a broader definition, it also covers materials with ferro- and antiferro- orders. There are significant scientific and technological interests in these materials due to their unusual responses, including very large magneto-electric susceptibility, giant magnetostriction, and energy coupling coefficients [11, 12]. In addition, the ability to couple between the spontaneous order parameters offers extra degrees of freedom in the design of conventional devices. Examples of single component multiferroics are $BiFeO_3$ (a ferromagnetic/ferroelectric perovskite), and Fe-Ga (a ferromagnetic/ferroelastic alloy).

1.2.1 Ferroelectric/antiferromagnetic $BiFeO_3$ (BF)

$BiFeO_3$ is one of the few single phase materials that exhibit both ferroelectric and antiferromagnetic properties at room temperature. It was first synthesized in 1957 by Royen and Swars. Numerous studies have been devoted to this compound motivated by multiferroic properties and the potential high magnetoelectric property.

Structure of $BiFeO_3$

The atomic structure of $BiFeO_3$ was determined by Michel et al. in 1969 [13], who performed x-ray diffraction on single crystal and neutron diffraction on powder samples. The space group was found to be R3c-C63v. The rhombohedral unit cell contains two formula units of $BiFeO_3$, owing to the oxygen shifts. The magnitude of ion shifts are Bi:

0.62 Å along [111]; Fe: 0.23 Å along [111]; O: 0.30Å along [111], all values ± 0.03 Å. The rhombohedral unit cell parameters are ar=5.61 Å and αr= 59°40'. The pseudo-cubic representation of these rhombohedral cell parameters are ac=3.96 Å and αc= 89°28'.

Any rhombohedral unit cell representation can be transformed to an equivalent hexagonal one. The magnetic and electrical properties of the BF crystal are often expressed in the hexagonal cell, the pseudo-cubic direction [111]c corresponding to the hexagonal [001]h. Fig 1.4 shows the hexagonal unit cell of BiFeO3. At room temperature, the cell parameters are ah=3.96 Å and ch= 13.9 Å [14, 15, 16].

Electrical properties of $BiFeO_3$

Bismuth ferrite undergoes a ferroelectric ordering along $[001]_h$ at a T_c of 830C°. The polarization is due to the cooperative distortion of the Bi^{3+} and Fe^{3+} cations from their centro-symmetric positions. The spontaneous polarization P_s is oriented along the pseudo-cubic $[111]_c$. Electrical characterization on bulk $BiFeO_3$ has been very difficult due to the low resistivity of samples. The controversy about whether it is ferroelectric or antiferroelectric was finally settled based on the hysteresis loop measured by Teague et al. [18], who performed experiments at liquid nitrogen in order to lower the charge carrier density and mobility, i. e. to reduce the leakage currents. The measured spontaneous polarization was reported to be 3.5μC/cm^2 along the <100> direction, which corresponding to 6.1μC/cm^2 along <111>. This value is much smaller than what would be expected for a ferroelectric material with such high Curie temperature and large c/a distortion.

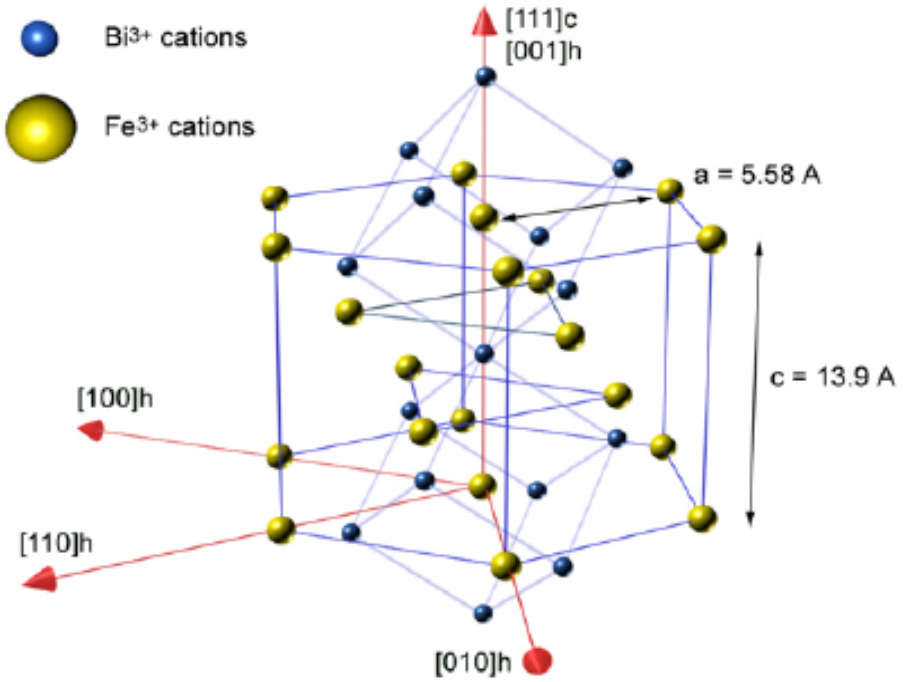

Figure 1.4 Hexagonal unit cell of $BiFeO_3$. Figure adapted from Ruette et al. [17]

However, recent investigation of single crystalline thin films fabricated by pulsed laser deposition (PLD) have shown a much higher P_s along the [001]c and [111]c, approaching values of 0.6 C/m^2 and 1.0 C/m^2 at room temperature respectively. The resistivity of these films were quite high, in the range of 10^9-10^{10} Ω·cm [19].

Magnetic properties of $BiFeO_3$

Single crystal of $BiFeO_3$ is an antiferromagnetic (T_N~643 K) with G-type spin structure. The spin is provided by the transition metal cation Fe^{3+}. In this arrangement, the Fe^{3+} cations are surrounded by six nearest Fe^{3+} neighbors, with opposite spin directions. The antiferromagnetic order is oriented along the $[001]_h/[111]_c$ and a spin rotation plane exists parallel to the $[110]_h$.

Microscopically, the antiferromagnetic spin order is not homogenous for $BiFeO_3$ single crystals. Precise neutron diffraction studies have revealed an incommensurately modulated spin structure which manifests itself as a cycloid with a long wavelength λ of ~600 Å [20, 21]. Its existence has also been confirmed by line shape analysis of nuclear magnetic resonance (NMR) spectra [22, 23]. In the incommensurate phase the periodicity of the spin polarization is incommensurate with crystallographic lattice parameters. The cycloidal spin structure has been shown to be directed along the $[110]_h$. A schematic picture of the spin rotation and spiral direction is shown in Figure 1.5.

As the antiferromagnetic vector is averaged to zero over λ, the induced magnetization under H is very small. However, application of high magnetic field (H>18Tesla) is known to induce a phase transition from the spatially modulated AFM

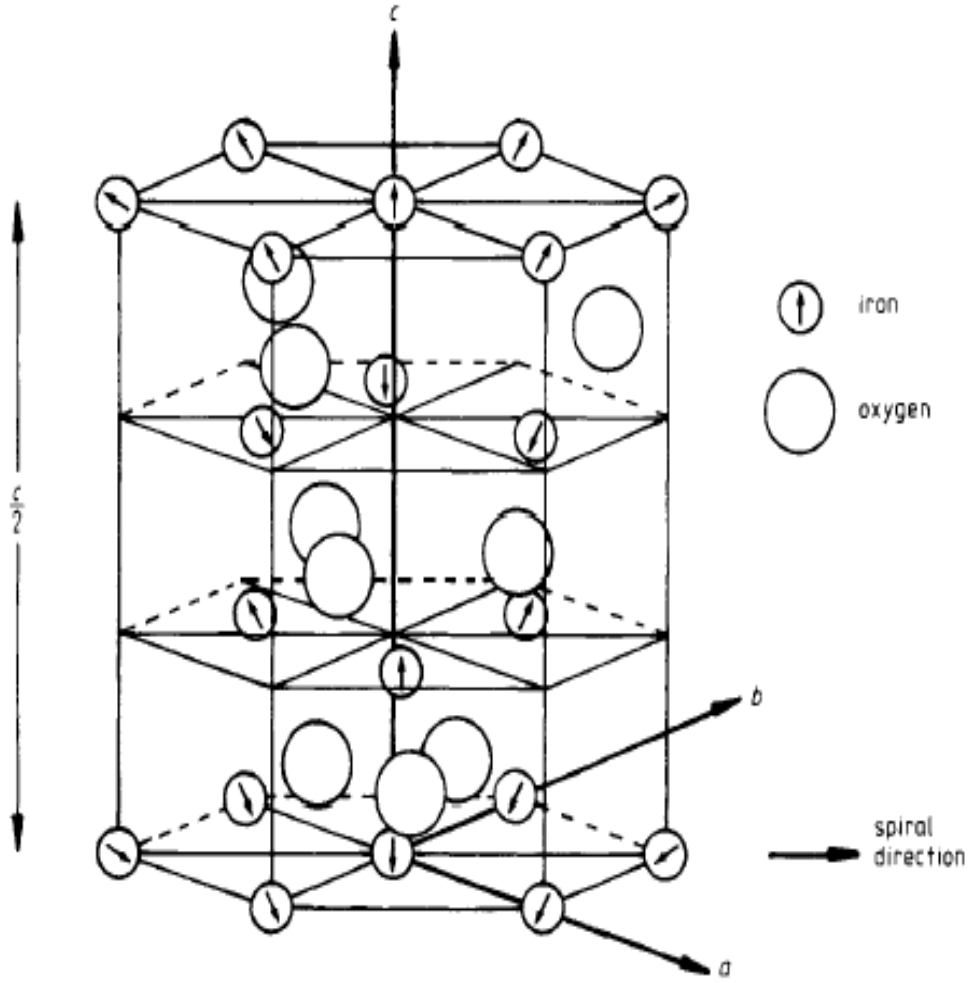

Figure 1.5 Portion of $BiFeO_3$ lattice. The arrows indicate the Fe^{3+} moment direction of the proposed model. The spiral period is reduced for illustration purpose. Figure adapted from Sosnowska et al. [20]

spin structure to a homogeneous one. In this case, the spiral is destructed by high magnetic field. It is also verified that the phase transition to spatially uniform antiferromagnetic state is accompanied with the onset of a linear magnetoelectric effect and a weak ferromagnetic moment [24, 25, 26].

$BiFeO_3$-$PbTiO_3$ solid solution

One of the major problems of BF is its low electrical resistivity, which has prevented practical application of the material. A further complication is that the coercive field E_c of $BiFeO_3$ is very high, making it an extremely difficulty to pole specimens into a ferroelectric state. To enhance the resistivity and lower Ec, recent work has focused on solid solutions of $BiFeO_3$ with other perovskites [such as $PbTiO_3$, $BaTiO_3$, $SrTiO_3$, and $Pb(Fe,Nb)O_3$] [27,28,29,30].

The $BiFeO_3$-$PbTiO_3$ (BF-PT) solid solution series were first reported by Venevstev et al. [31]. They observed that the tetragonal phase persisted in the series from the PT end member up to 70 wt% BF, and that a large c/a ratio presented in the tetragonal phase around 60 wt% BF. Subsequent work by Fedulov et al. [32] demonstrated the existence of a morphotropic phase boundary (MPB) between 66 wt% and 73 wt% BF, within which rhombohedral (R) and T phases coexist, as shown in Fig.1.6. Smith et al. measured the T_c of BF-PT as a function of BF content, which gave further support of the ferroelelctriciy of BF. However, the measurement was conducted using a high measurement frequency of 0.53GHz [29].

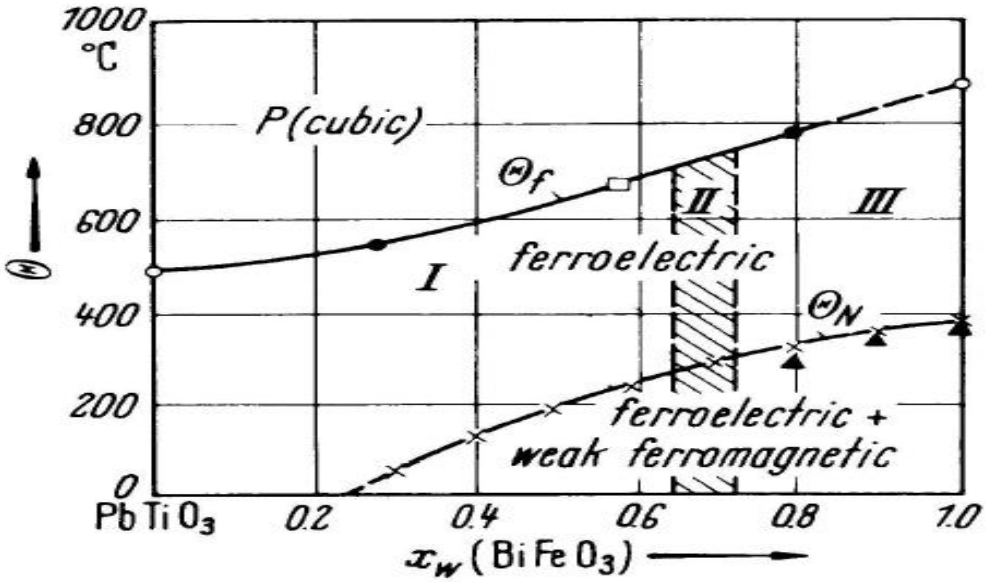

Figure 1.6 $BiFeO_3$-$PbTiO_3$ phase diagram [32].

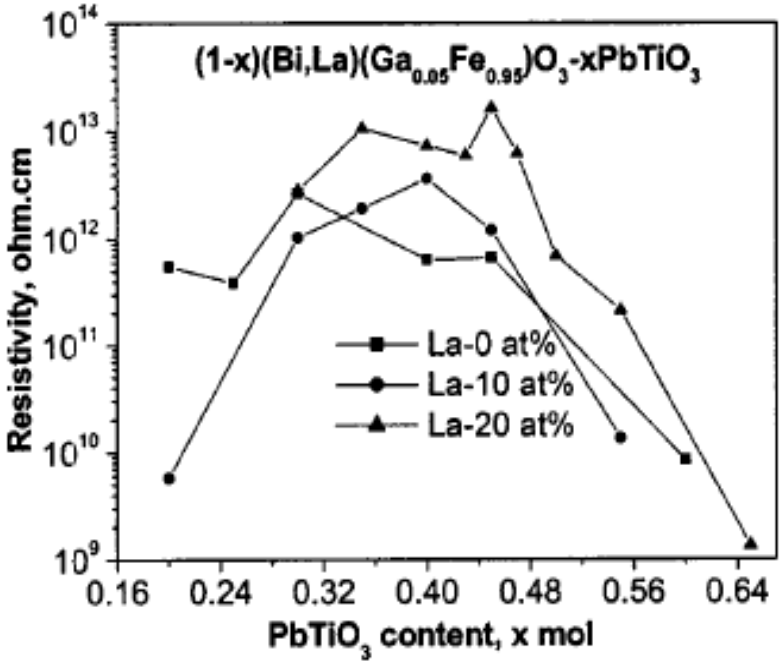

Figure 1.7 Electrical resistivity of BLGF-PT as a function of PT content for various La concentrations as at room temperature [35].

Recently, Chen and Cross reported a significant enhancement in the insulated resistivity of BF-PT by gallium dopants (BGF-PT) [36]. A small amount of gallium substituted to iron decreased the loss factor at low frequencies. Subsequently, modified BF-PT with Ga and La (BLGF-PT) revealed an even higher resistance [37]. As shown in Fig. 1.7, in the vicinity of the MPB region, the resistivity reaches values of up to 10^{12}-10^{13} Ω·cm. In addition, significantly enhanced dielectric and piezoelectric properties were achieved for BLGF-PT in the vicinity of the MPB.

1.2.2 Ferromagnetic/Ferroelastic Fe-Ga single crystal

Magnetostrictive materials

Magnetostrictive materials exhibit reversible strains and elastic property changes in the presence of an applied magnetic field, or the reciprocal effect of changes in the magnetic properties when applied stress. While magnetostriction is observed in all ferromagnetic materials, these that exhibit large Joule magnetostriction at low field, are of interest for use as acoustic sensors and generators, linear motors, actuators, damping devices, torque sensors, positioning devices, speakers, and microphones [36].

Joule magnetostriction is the shape change of a ferromagnetic material increased with a change in magnetizaion. The value measured at magnetic saturation is called the saturation magnetostriction λs. It can be calculated by the equation: $\lambda s = \Delta l / l$, where the quantity l represents the sample length.

The earliest magnetostrictive alloys used in engineering applications were nickel-

based alloys with saturation magnetostriction values of about 50×10^{-6}. In the 1960s, rare earth materials were found, which had much larger magnetostriction (λ_{100}=1000μ). Rare earth elements Dy and Tb have giant magnetostrictive strains of about 1%, at cryogenic temperatures, but also exhibit appreciable hysteresis [37, 38]. Large room temperature magnetostriction values have been reported for RFe_2 intermetallic compounds (where R refers to rare-earth elements) such as Terfenol alloys with a composition $(Dy_xTb_{1-x})Fe_2$. These alloys with a cubic *C*15 structure have high Neel temperatures and show magnetostrictive strains on the order of 0.1 % at 300K. A widely used Terfenol alloy is Terfenol-D with a composition $Dy_{0.7}Tb_{0.3}Fe_2$. In this alloy, the relative amounts of Dy and Tb have been optimized to minimize the fourth order anisotropy at room temperature. However, Terfenol-D alloys are brittle, require large fields for saturation and are expensive due to the high costs of Tb and Dy. On the other hand, amorphous Metglass alloys such as $Fe_{81}B_{13.5}Si_{3.5}C_2$ require low fields for saturation, but have a low saturation magnetostriction of about 30×10^{-6}.

Magnetostrictive materials that have high mechanical strength, good ductility, large magnetostriction at low saturation fields, high imposed-stress levels, and low costs, are of current interest. Recently, Fe–Ga alloys produced by conventional material fabrication processes have been thought to meet all these expectations.

Materials with large magnetostriction are listed in Table II.

Table II Materials with large magnetostriction

	Magnetostrictive Strain [$^{-6}$10]	Explanation	Mechanical property	Price
Ni	-58.3	Joule Magnetostriction	Ductile	Inexpensive
Fe	20	Joule Magnetostriction	Ductile	Inexpensive
$Fe_{84}Al_{16}$	86	Joule Magnetostriction	Ductile	Inexpensive
$Fe_{83}Ga_{17}$	207	Joule Magnetostriction	Ductile	Inexpensive
$Fe_{60}Co_{40}$	147	Joule Magnetostriction	Brittle	Inexpensive
FeTbDy	1,600	Joule Magnetostriction	Brittle	Expensive
NiMnGa	50,000	Reversible strain resulting from the	Brittle	Medium

Magnetostriction of Fe-Ga alloys

Clark et al. [39, 40] reported a large magnetostrictive strain of λ_{100}>200ppm at room temperature in Fe-Ga (or Galfenol) single crystals, which is ~10x that of pure Fe. A similar finding was reported earlier by Hall [41], whom found that the addition of Al to Fe enhanced λ_{100} by ~4x. These reports demonstrate that the magnetostriction of Fe can be dramatically enhanced by substitution of non-magnetic elements, i.e., λ_{100} increases even though the saturation magnetization (M_s) decreases. The solubility of Ga in α-Fe is known to be large – up to 36at% at 1300K. The value of λ_{100} has been reported [42] to increase with increasing Ga content, reaching a maximum for x~17-19at%, subsequently decreasing sharply for 22<x<23at%; however, a second maximum in λ_{100} occurs in the

composition range of x=27at%Ga, as shown in figure 1.8. Upon quenching, the peaks were shifted to higher Ga content, and the magnetostriction was enhanced.

The disordered BCC structure of the A2 phase is maintained in the Fe-x%Ga solution for x<15at% [43, 44]. For 15<x<22at%Ga, the A2 structure is thought not to be the equilibrium phase, although this structure can be maintained by rapid quenching from ≥1075K until x≈19at% [39,40,42,44,53]. In this compositional range, the stable phase in the slow-cooled condition has been reported to have a partially ordered DO_3 structure. For x>22at%, the alloys become fully DO_3 ordered [43-49], as shown in figure 1.9. Ordering is believed to result in a body-centered tetragonal (BCT) unit cell with lattice parameters of $a_t=b_t=4.1$Å and $c_t=2.9$Å [7], which is believed to be essentially cubic as $a/c \approx \sqrt{2}$ [44]. Thus, it is expected (i) that only the DO_3 phase (x>20at%) should have a tetragonal splitting induced by Ga ordering; and (ii) that the tetragonal distortion should be too small to be detectable.

The enhancement of magnetostriction has been interpreted based on a model of pairing of Ga atoms along $(001)_c$ axis. This model successfully explains the anisotropy of magnetostriction. Ab-initio calculations have then indicated that a tetragonal structure – induced by the short-range ordering of Ga atoms – is important to enhanced magnetostriction [51]. This structure has not yet been experimentally verified either by x-rays or neutron diffraction. The ab-initio approach also assumes that the structure is homogeneous on the micro-scale, as well as on the macro-scale. However, recent magnetic force microscopy (MFM) studies of Fe-x%Ga [52] have revealed the presence of miniature domains on the size of ≤1000Å for x≥20at%, indicating that inhomogeneity

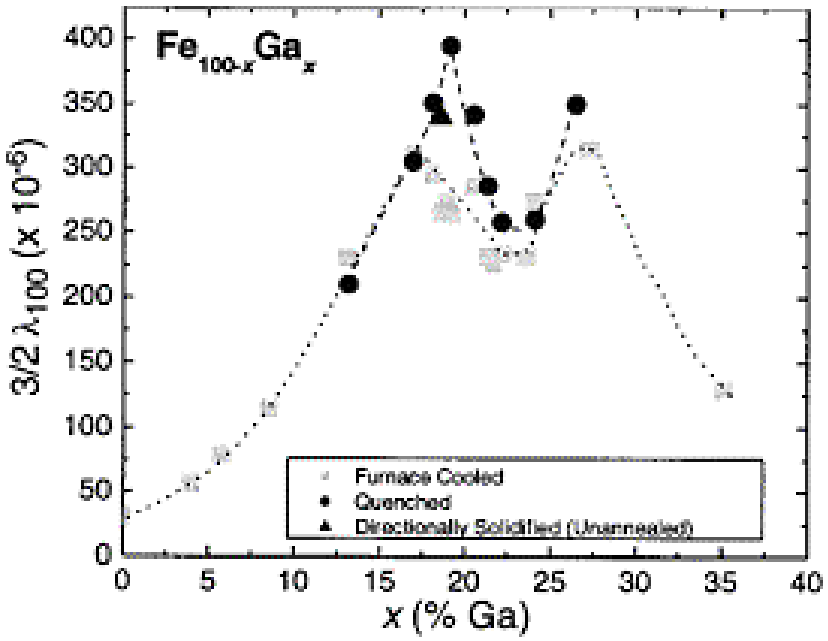

Figure 1.8 (3/2) λ_{100} as a function of Ga concentration for $Fe_{100-x}Ga_x$ [42]

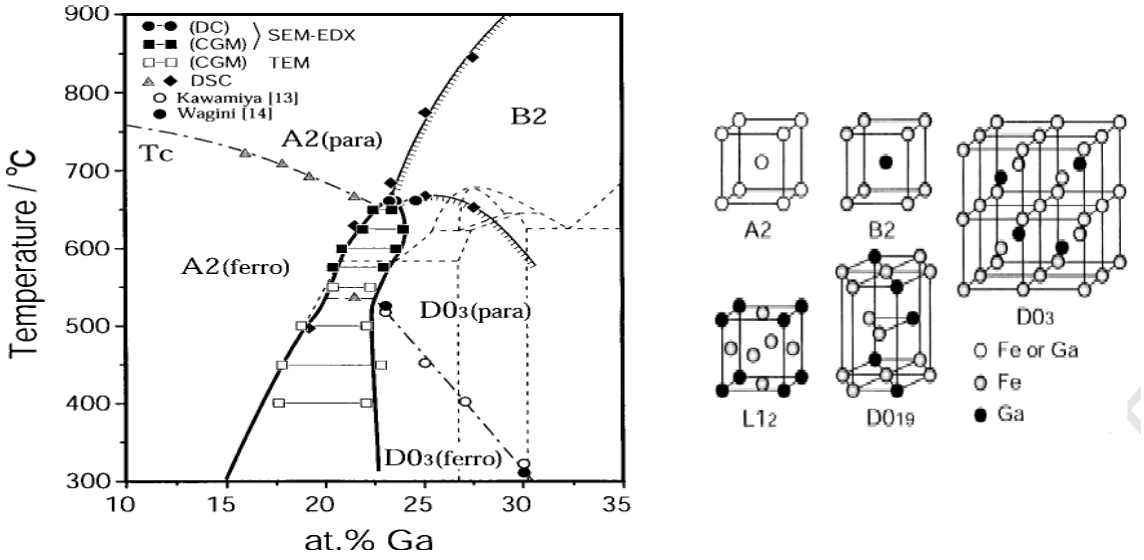

Figure 1.9 Phase diagram of Fe-Ga alloy and the crystal structures of A2, B2, DO_3, $L1_2$ and DO_{19} [53].

on the microscale may play an important role in enhanced magnetostriction. In addition, structural studies of Fe-19%Ga using a triple-axis diffractometer [50] have revealed a cubic structure with notable transverse line broadening in (002) mesh scans, indicating a short lateral correlation length.

CHAPTER 2 PURPOSE OF RESEARCH

In this thesis, I will present results from structure-property relationship investigations of two multiferroic crystalline solutions, which are (i) modified $BiFeO_3$-x%$PbTiO_3$ ceramics that are ferroelectric and antiferromagnetic; and (ii) Fe-x%Ga single crystals that are ferroelastic and ferromagnetic alloys. Investigations have been performed using a variety of macroscopic property probes such as (i) magnetization versus magnetic fields (M-H); (ii) polarization versus electric fields (P-E); (iii) dielectric constant, and (iv) magnetic permeability; and microscopic structural probes such as x-ray and neutron diffraction. Specifically, I will show

(1) studies of the ferroelectric and ferromagnetic properties of La-Modified $BiFeO_3$-x%$PbTiO_3$. It will be shown that a weak ferromagnetic state is induced by La substitution from an antiferromagnetic spin cycloid [see Chapter 3-Section 3.2];

(2) that a maximum in the magnetic permeability is induced by La substituent in $BiFeO_3$-x%$PbTiO_3$, indicating a relaxational magnetization [see Chapter 3-Section 3.3] ;

(3) structural studies of Fe-x%Ga for $12 \leq x \leq 25$ by x-ray and neutron diffraction. These studies reveal (i) a tetragonal splitting along the (002) direction for x=12 and 25at%, but only a single broad averaged-cubic peak for x=20at%; and (ii) a splitting transverse to the (002), revealing a domain texture in which domains are slightly tilted with respect to each other, and whose pattern changes with x [see Chapter 4] .

CHAPTER 3 MULTIFERROIC PROPERTIES OF MODIFIED $BiFeO_3$-X%$PbTiO_3$ BASED CERAMICS

Although promising, the multiferroic properties of either $BiFeO_3$ crystals or ceramics require too high of fields to be considered practical. In particular, it is important that the magnetic field required to induce the transition between canted and uncanted spin states be dramatically lowered. In this investigation, we report the multiferroic properties of modified $BiFeO_3$-$PbTiO_3$ ceramics (BLGF-PT). For comparison, we also studied the magnetic properties of unmodified $BiFeO_3$ single crystal. It has been found that aliovalent substituted $BiFeO_3$-$PbTiO_3$ based ceramics have significantly enhanced multiferroic properties. Relative to unmodified $BiFeO_3$ single crystal, our results for modified $BiFeO_3$-$PbTiO_3$ based ceramics reveal: (i) a dramatic increase in the induced polarization; (ii) a dramatic decrease in the field required to induce a transition between canted and uncanted spin structures, and a resultant enhancement in the induced magnetization; and (iii) the establishment of a remnant magnetization. The results evidence a breaking of the translational invariance of a long-period cycloidal spin structure, via substituent effects.

In addition, temperature dependent magnetic permeability of BLGF-PT crystalline solutions was investigated. The results have shown that aliovalent substitution results in (i) a significant increase in the permeability, relative to BF single crystals; by inducing (ii) a diffuse magnetic→magnetic phase transition that has superparamagnetic-like characteristics.

3.1 Experimental Procedure

Traditional mixed oxide ceramic processing was utilized for the production of solid solution of (Bi, La)(Ga, Fe)O_3-x%$PbTiO_3$. Starting materials were commercial reagent-grades of Bi_2O_3, Fe_2O_3, Ga_2O_3, La_2O_3, $PbCO_3$, and TiO_2 with 99%+ purity. We have fabricated ceramics of La-modified Bi(Fe,Ga)O_3-x%$PbTiO_3$, with La concentrations of 10, 20, 30, 40 at% and for x=45. Raw materials were batched stoichiometrically, accounting for combustion and hydration losses. The oxides were mixed by ball milling for 24 hours with stabilized ZrO_2 media and dried at 70°C. The raw powders were then calcined in open crucible to achieve perovskite phase formation. A double calcinations route was utilized to improve mixedness and the phase purity of the final product. Powders were calcined at 750°C for 4 hours. Following each calcinations, powders were milled and dried as above. To improve the green strength of compacts, and addition of 3-5wt% of Polyvinyl alcohol solution system was thoroughly mixed with these powder as binder. This mix was dried and sieved. Pellets were loosely pressed under uniaxial pressure in a 13 mm die and cold isostatic pressed at 150 MPa. Following a 500°C binder burnout, pellets were sintered at 1000-1120°C for 0.8 hours in a sealed crucible, using a source powder of similar composition with excess additions of volatile species. Weight loss of pellets was confirmed to be below 2%. The specimen dimensions were 10.4 mm in diameter and 0.5 mm in thickness.

$BiFeO_3$ single crystals were grown by a flux method from a Bi_2O_3-Fe_2O_3-Nacl melt. Single crystals were oriented along the [001]c. Crystals were cut into dimensions of $1\times1\times0.5$ mm^3.

Phase determination for calcined powders and sintered pellets were made using x-ray diffraction (PAD V and X2 diffractometers, Scintag) and DMSNT (Scintag) data collection and analysis software.

For electrical characterization, ceramic specimens were electroded using a post-fired silver paste (Dupont 6160). Some of the disks were poled in a 120^{o}C oil bath at 40 kV/cm for 10 minutes. Dielectric measurements were carried out for 300<T<600^{o}C using a computer controlled HP4284. Ferroelectric hysteresis loops (i.e., P-E response) were measured using a modified Sawyer-Tower circuit.

The DC magnetization loops (i.e., B-H response) were characterized as a function of H at various temperatures using a superconductive quantum interference device (SQUID) magnetometer (Quantum Design, model XL7). Before magnetization measurements were performed, the electrodes were removed from the specimens.

The magnetic permeability was characterized as a function of temperature using a SQUID magnetometer (Quantum Design, model XL7). Measurements were made using an ac magnetic drive of H_{ac}=5 Oe, at frequencies between 1-10^3 Hz.

3.2 Ferroelectric and ferromagnetic properties

3.2.1 Ferroelectricity

Two of the main problems of $BiFeO_3$-based materials that have previously limited development are (i) a low resistivity ρ which has made it difficult to obtain good pole. The resistivity of our specimens was on the order of 10^{12} Ω·cm. Consequently, the dielectric properties could be measured. The composition $(Bi_{0.8}La_{0.2})(Fe,Ga)O_3$-45%$PbTiO_3$, which is close to a morphotropic phase boundary [54, 55], had a room temperature dielectric constant K and tanδ (10^3 Hz) of 1800 and 2.4%, respectively. Figure 3.1 shows the dependence of K on temperature (T) for this composition. The value of T_c was ~500K. It is important to note that the temperature dependent response revealed a broad transition region. Also, measurements at various frequencies showed relaxor characteristics [56], indicative of underlying polarization nonuniformity.

The ferroelectric polarization behavior was then investigation. It was found that E_c was pronouncedly decreased to <30 kV/cm for our modified ceramics, which is much lower than previous reports of >100 kV/cm. Figure 3. 2 shows the P-E loops. A non-linear P-E relationship can be seen for E≈30 kV/cm. Saturation of the P-E loop occurred near E≈50 kV/cm, with values of P_r and E_c of 20 μC/cm^2 and 60 kV/cm, respectively. Conductivity effects were not notable in the P-E loops. These results clearly demonstrate that our modified $BiFeO_3$-$PbTiO_3$ based ceramics can be poled into a ferroelectric state that has remnant and saturation polarizations, which are nearly an order of magnitude higher than that of unmodified $BiFeO_3$ crystals.

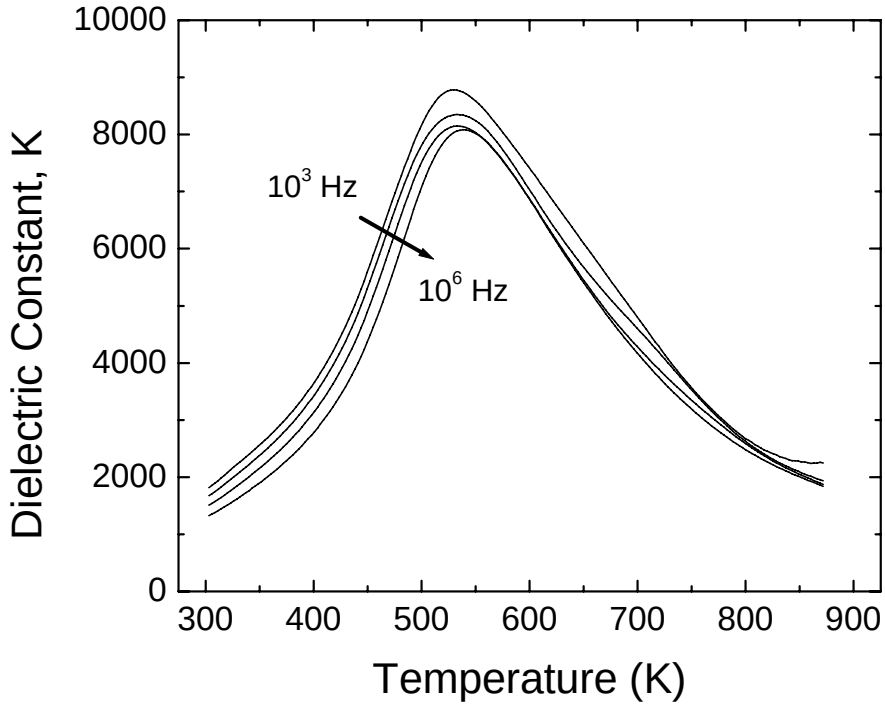

Figure 3.1 Dielectric constant of $(Bi_{0.8}La_{0.2})(Fe,Ga)O_3$-45%$PbTiO_3$ as a function of temperature. Data are shown for measurements taken at frequencies of 10^3, 10^4, 10^5, and 10^6 Hz. dielectric properties.

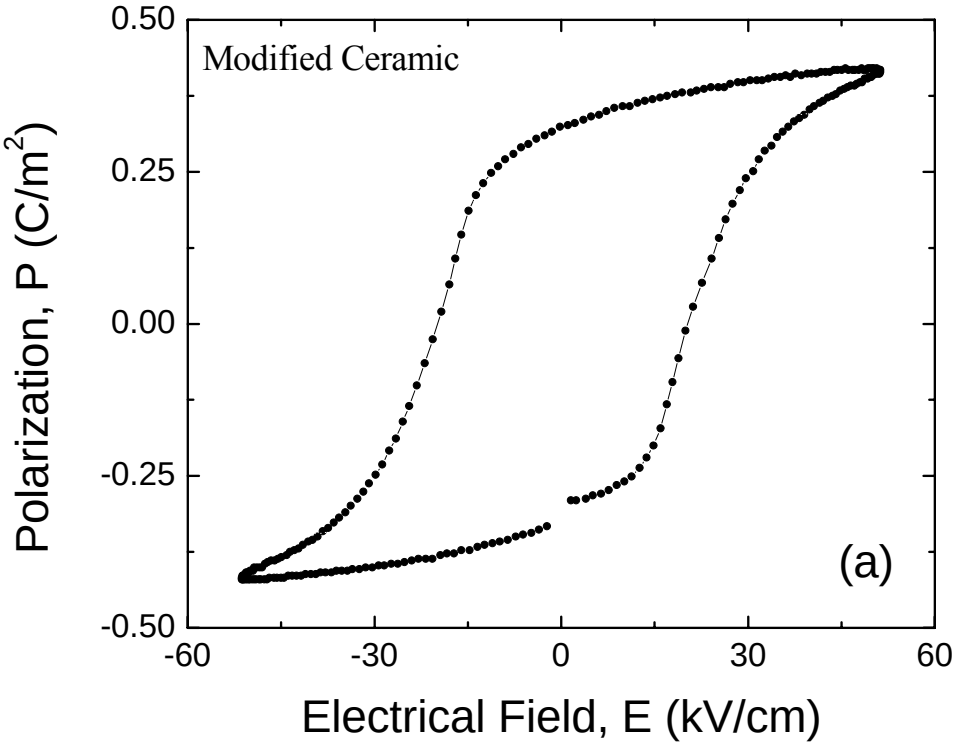

Figure 3.2 Induced polarization as a function of electric field E for $(Bi_{0.8}La_{0.2})(Fe,Ga)O_3$-45%$PbTiO_3$ ceramics.

3.2.2 Ferromagnetization

Next, the magnetization behavior was measured at T=300K. Figure 3.3 shows the M-H response for our modified $BiFeO_3$-$PbTiO_3$ based ceramics, along side that of a $BiFeO_3$ crystal. The single crystal exhibited a near linear M-H relationship for $H<7x10^4$ Oe. The value of the induced magnetization at this high field level was <0.4 emu/g.

However, for our modified $BiFeO_3$-$PbTiO_3$ based ceramics, a larger magnetization was found at dramatically lower H. A ferromagnetic hysteresis loop can be seen in this figure which has a remnant magnetization, saturation magnetization, and coercive field of 0.3 emu/g, 0.6 emu/g, and $3x10^3$ Oe respectively. These results clearly demonstrate that our $BiFeO_3$-$PbTiO_3$ based ceramics can be poled into a ferromagnetic state that has remnant and saturation magnetizations higher than that of unmodified $BiFeO_3$ crystals.

Finally, the magnetization behavior was measured at T=5K for both a modified $BiFeO_3$-$PbTiO_3$ based ceramic and a $BiFeO_3$ crystal. Figure 3.4(a) shows the M-H response for the $BiFeO_3$ single crystal (data for T=300K is shown for comparisons). The M-H behavior can be seen to be temperature independent between 5<T<300K, over the field range investigated. However, the magnetization behavior of our modified $BiFeO_3$-$PbTiO_3$ based ceramic was found to be notably temperature dependent. Figure 3.4(b) shows the M-H response for the ceramic taken at both T=5 and 300K. The saturation and remnant magnetization were both increased on cooling to T=5K; however, interestingly, the coercive field was decreased with decreasing temperature. For T=5K, the values of

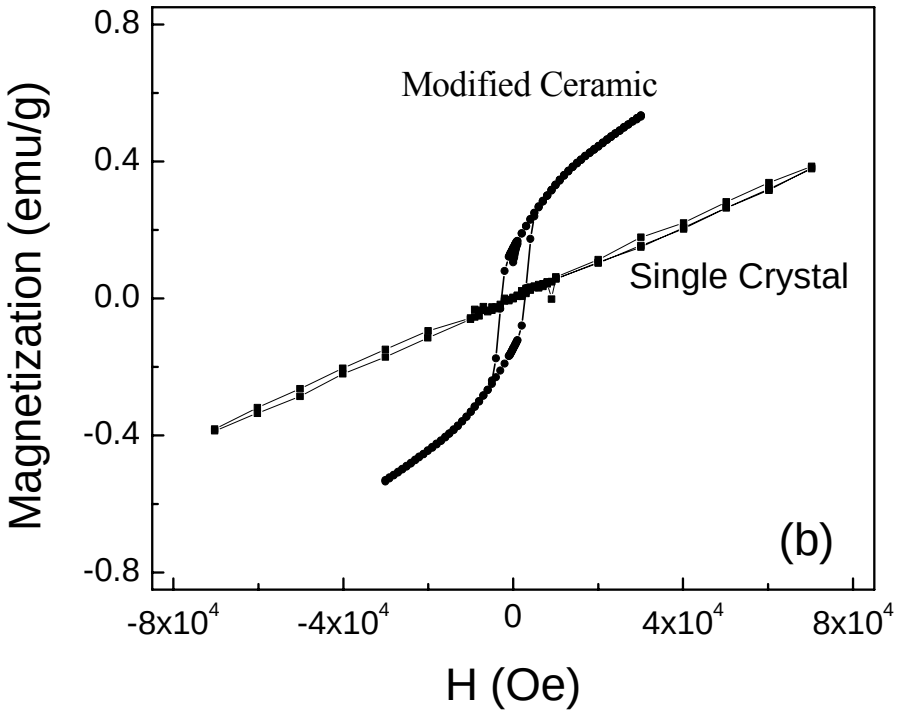

Figure 3.3 Induced magnetization as a function of magnetic field H for $(B_{i0.8}La_{0.2})(Fe,Ga)O_3$-43%$PbTiO_3$ ceramics, corresponding single crystal data is shown for comparisons. These data were all taken at T=300K.

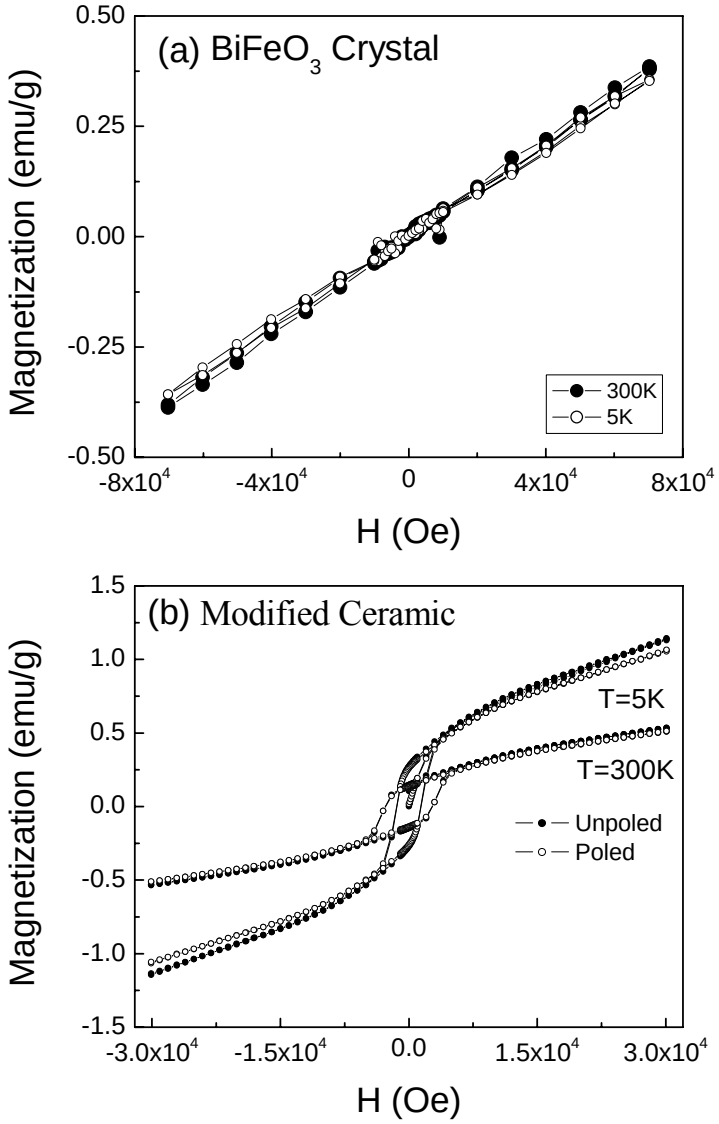

Figure 3.4 Effect of temperature and electrical poling on the induced magnetization as a function of magnetic field H. (a) $BiFeO_3$ single crystal in the electrically unpoled condition. Data are shown in both figures for T=5 and 300K; and (b) $(Bi_{0.8}La_{0.2})(Fe,Ga)O_3$-45%$PbTiO_3$ ceramic, in both the electrically poled and unpoled conditions.

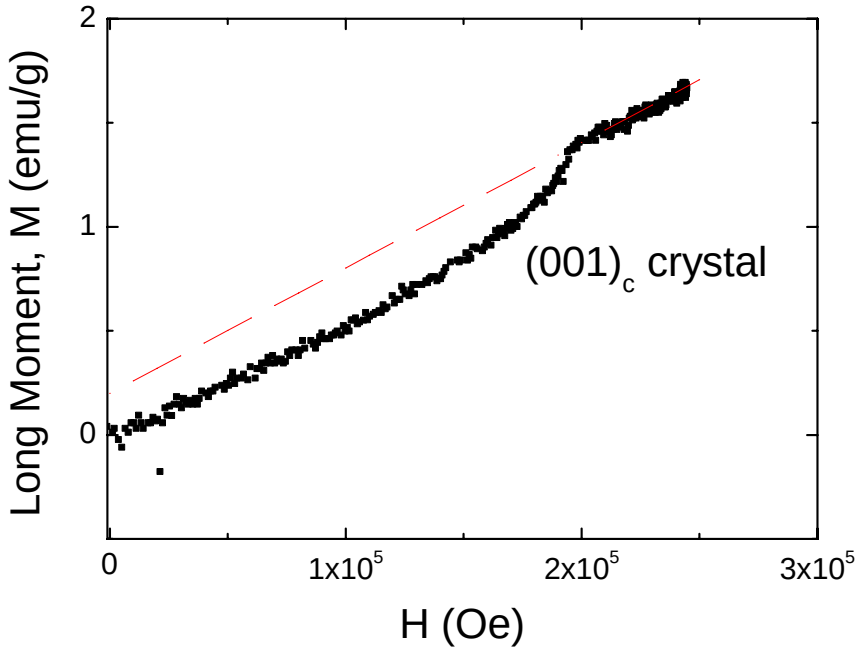

Figure 3.5 The field dependence of $BiFeO_3$ magnetizaiton at 10K [56].

the remanent magnetization, saturation magnetization, and coercive field were 0.5 emu/g, 1 emu/g and $1.5x10^3$ Oe, respectively. It is also important to note in Figure 3.4(b) that both electrically unpoled and poled specimens yielded similar M-H responses. The results in Figure 3.4 clearly demonstrate an important difference in the temperature dependent magnetization between $BiFeO_3$ crystals and modified ceramics. The results show that the exchange coupling is nearly temperature independent for crystals, but is quite temperature sensitive for our modified ceramics.

Recent investigations of the magnetization of $BiFeO_3$ crystals under high pulsed magnetic fields of $H \leq 20$ Tesla [56], for T=5K, have demonstrated an induced transition in the M-H response, with a saturation magnetization of ~0.7 emu/g, as shown in Figure 3.5. This is the cycloidal to homogeneous spin transition [48-51]. Comparisons of these results [56] to that in Figure 3 evidence that the magnetic field required to induced the transition between canted and uncanted spin structuress is dramatically decreased by substituent modifications in ceramics.

3.2.3 Discussion

Microscopically, the antiferromagnetic spin order of $BiFeO_3$ single crystals is not homogeneous. Rather, an incommensurately modulated spin structure is present [21], which manifests itself as an incommensurate spiral with a long wavelength λ of ~600 Å [20,21,49-51]. The spin spiral is directed along the $[110]_h$, and is dependent on applied magnetic field and temperature [52]. Breaking of the translational symmetry of the spiral

spin modulation might be achieved by substituent effects in perovskites which have ferroelectric and antiferromagnetic orders [52-54]. We can understand these changes by the Landau-Ginzburg (LG) formalism for the free energy [49], given as

$$F = F_L + F_{exch} + F_{an} + F_m; \tag{2}$$

where F_L is the magnetoelectric coupling that is linear in gradient (i.e., Lifshitz invariant), F_{exch} is the inhomogeneous exchange energy, F_{an} is the magnetic anisotropy energy, and F_m is the magnetic energy. The individual terms in the sum of (2) have previously been given in [49, 64].

To understand the influence of substituents, we add the random-field perturbation, $H_{RND}=\beta \cdot P_{RND}$, to F_{an} given as

$$\Delta F_{an} = -r \cdot \sum_{r=1}^{N} \left(\chi_{\perp} \frac{(\beta \cdot P_{RND})^2}{2} \sin^2 \theta(\vec{r}_i) \right); \tag{3}$$

where θ is the polar angle, $\chi_{\perp}$ is the magnetic susceptibility in the direction perpendicular to the antiferromagnetic vector, β is the magnetoelectric coefficient of the homogeneous spin state, and P_{RND} is a random-field induced polarization change. It is important to note that only charged imperfections give significant contributions to the magnetic anisotropy energy, and that coupling between the spin spiral and defects is mediated only by magnetoelectric interactions. The summation in (3) is taken over all pinning centers and anisotropy axes. The ratio r in (3) is $r = \frac{b^3}{V} = \frac{1}{N}$, where b is the characteristic volume of the pinning center, V is the unit volume, and N is the number of pinning centers per unit volume. The volume-averaged LG free energy density of the

cycloid ($F_{cycloid}$) that takes into account all terms in (2) can be derived following [50], as

$$F_{cycloid} = -\frac{\gamma \cdot P_z}{2} q + Aq^2 + \frac{K_u'}{2} - \frac{\chi_\perp (\beta \cdot P_{RND})^2}{2} \left\langle \sin^2 \theta \right\rangle_V ; \quad (4)$$

where q is the wave vector of the modulation, A is the stiffness constant of the cycloid, γ is the inhomogeneous magnetoelectric constant, β is the magneto-electric constant of the homogeneous spin state, and $\langle ... \rangle_V$ means averaging over volume. The term $K_u'/2$ in (4) designates the unperturbed part of the uniaxial anisotropy energy, averaged over the period of the spiral ($\left\langle \sin^2 \theta \right\rangle_\lambda = \frac{1}{2}$). The effective anisotropy constant K_u' is treated as a sum of the uniaxial anisotropy K_u and a magneto-electrical term, i.e., $K_u' = K_u - \frac{\chi_\perp (H_{ME})^2}{2}$, where $H_{ME} = \beta \cdot P_z$ is the magnetic field induced by the spontaneous polarization P_z due to magnetoelectric interaction. By replacing the sum in (3) with an integral over the volume, and by minimizing (4) for $q = \frac{\alpha \cdot P_z}{4A}$, we obtain the volume-averaged free-energy as

$$F_{cycloid} = -\frac{1}{16A} (\gamma \cdot P_z)^2 + \frac{K_u}{2} - \frac{\chi_\perp (\beta \cdot P_z)^2}{4} - \frac{\chi (\beta \cdot P_{RND})^2}{3} . \quad (5)$$

The spiral is destroyed when the free energy (5) of the space modulated state is equal to the energy of the nonspiral state

$$F_{Nonspiral} = K_u - \chi_\perp \frac{(\beta \cdot P_z)^2}{2} - \chi_\perp \frac{(\beta \cdot P_{RND})^2}{2} , \quad (6)$$

which occurs when the following conditions for the substituent perturbation $\beta \cdot P_{RND}$ is fulfilled

$$\chi_{\perp} \frac{(\beta \cdot P_{RND})^2}{6} > \frac{K_u}{2} + \frac{(\alpha \cdot P_z)^2}{16A} - \frac{\chi_{\perp}(\beta \cdot P_z)^2}{4}. \quad (7)$$

Substituting values of $\chi_{\perp} = 4.7x10^{-5}$, A=8·10^{-7} erg/cm, $\gamma \cdot P_z = 4Aq$, $q = \frac{2\pi}{\lambda}$, $\lambda = 620\,\mathring{A}$, $K_u = 6.6 \cdot 10^5 \frac{erg}{cm^3}$ and β·P_s=1.2x10^5 Oe, we can estimate β·P_{RND}~10^6 Oe.

Approximating the values of β^{-1} and K using those of the homogeneous spin state (i.e., β^{-1}=3.3 V/cm-Oe and K≈100 [64]), we can now estimate the polarization change caused by introduction of substituents as

$$P_{RND}=0.3\ C/m^2. \quad (8)$$

It is equally important to estimate the equivalent random-field induced magnetization change m_{RND}, resulting from a coupling to P_{RND} through the linear magnetoelectric coefficient. This can be approximated as

$$\beta \cdot P_{RND} = \frac{m_{RND}}{\chi_{\perp}},$$

$$\text{or,} \qquad m_{RND} = \chi_{\perp}\beta \cdot P_{RND} = 0.47\ \text{emu/g}. \quad (9)$$

Accordingly, it is important to note that the induced polarization (ΔP) and magnetization (Δm) of our La-modifed $BiFeO_3$-$PbTiO_3$ materials was measured to be ΔP≈0.4 C/m^2 and Δm≈0.5 emu/g, as shown in Figures 2(a) and (b) respectively. These are in close agreement with the predicted values of P_{RND}+P_z and m_{RND}, which are both much greater than those of the unmodified $BiFeO_3$ crystals.

These results indicate that the homogeneous spin state is favored by large polarization changes. Such a large polarization change can not be understood by a simple dipolar defect model, but rather must reflect important changes in the spontaneous polarization and consequently ferroelectric stability. An important consideration emerges upon examination of P_s of $BiFeO_3$ crystals, as previously noted: the parent compound of our crystalline solution has a P_s that is significantly smaller than what might normally be expected for a ferroelectric with such a high T_c (for example, $PbTiO_3$, with T_c=763 K and a P_s=80-100 $\mu C/cm^2$). Rather, we conjecture that ferri-electric order may prevent the manifestation of a full spontaneous polarization, resulting in significant cancellation of polar vector moments. Introduction of substituents into a ferri-electric could then result in dramatic changes in P_s, by favoring a ferroelectric order.

In turn, following equation (9), a significant increase in P_s will be accompanied by a proportional change in the magnetization, via the linear magnetoelectric effect. In the spiral spin state, the projection of the antiferromagnetic vector is averaged out. However, substituents pertubate the spiral spin structure, via magneto-electric interactions that couple to the change in P_s. This results in a non-zero projection of the antiferromagnetic vector, and the release of the latent projection of the antiferromagnetic vector, which is trapped within the cycloid.

3.3 Magnetic permeability

3.3.1 Results

The temperature dependent magnetic permeability (μ') is given in Figure 3.6(a) for both the aliovalently modified ceramic and $BiFeO_3$ single crystal specimens. These data were taken using a measurement frequency of 1Hz. The single crystal can be seen to have a permeability value of $\mu' \sim 3x10^{-5}$ emu/g. It had a near featureless response to temperature changes over the range of $5<T<300K$. These results are in distinct comparisons to those for La-modified BF-PT ceramics, which can be seen in the figure to have (i) a significantly higher permeability of $\mu' \sim 5x10^{-4}$ emu/g; and (ii) a peak in the permeability at about T=135K, which had diffuse or broad temperature dependent characteristics. Figure 3.6(b) shows the corresponding imaginary (μ'') component of the magnetic permeability as a function of temperature for $5<T<300K$ for both specimens. The value of μ'' can be seen to be significantly higher for the aliovalently modified ceramic, relative to the crystal. Evidence of a phase transition in the aliovalent ceramic was also found in μ'', as a significant increase in the magnetic absorption can be seen in the vicinity of the peak in μ'. Clearly, both the real and the imaginary components of the permeability indicate a magnetic phase transition near T=135K for the aliovalently modified ceramic. This is not a transition to the paramagnetic state with increasing T, as the value of μ'' remains high for T>150K. Also, it is important to note at lower temperatures that the value of μ'' was decreased significantly, becoming nearly temperature independent for T<50K.

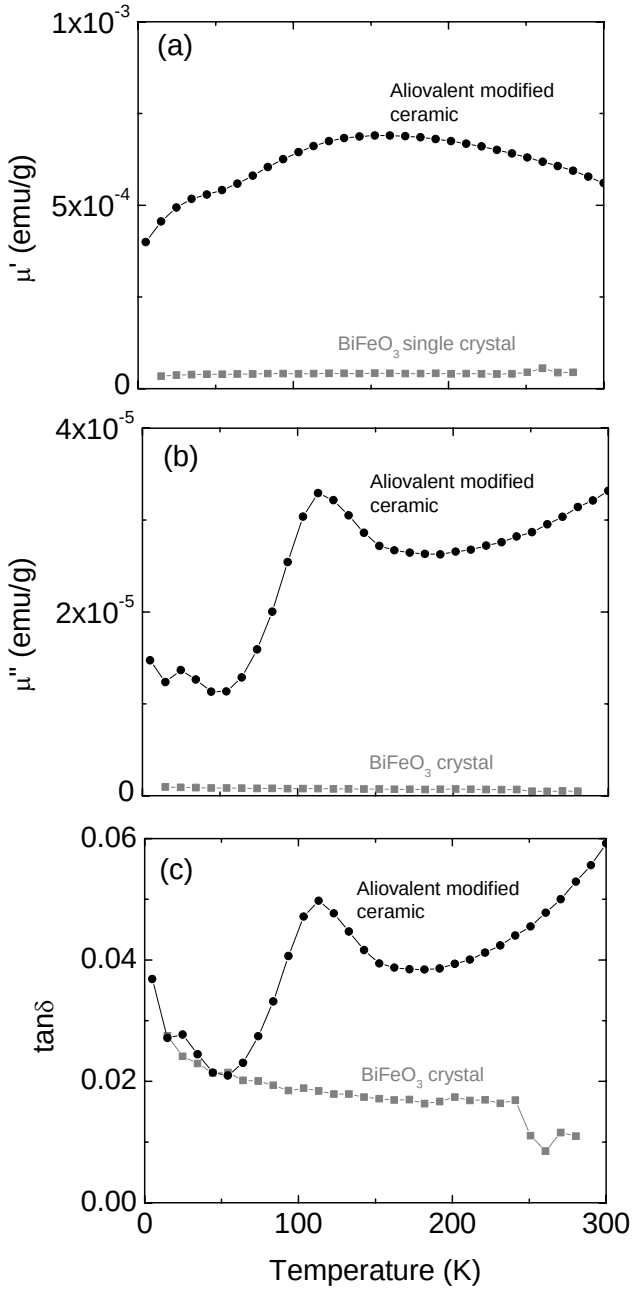

Figure 3.6 Temperature dependent magnetic permeability characteristics of aliovalent-modified BFO-43%PT ceramic and $BiFeO_3$ single crystal (a) real component; (b) imaginary component; and (c) phase angle or tanδ. This data was taken at a measurement frequency of 1 Hz, and an AC drive amplitude of 5 Oe.

To obtain more insight into the difference between the aliovalently-modified ceramic and $BiFeO_3$ crystal, we next determined the magnetic tanδ from the complex magnetic permeability, i.e., tanδ=μ''/μ'. Figure 3.6(c) shows tanδ as a function of T for both specimens. Interestingly, at lower temperatures of T<50K, the aliovalently modified ceramic and single crystal had nearly identical tanδ values. However, with increasing T, the value of tanδ increased significantly for the aliovalently modified ceramic, whereas that for the $BiFeO_3$ crystal was nearly unchanged with T. These results clearly demonstrate a common loss mechanism at lower temperatures for both specimens. However, for the aliovalently modified ceramic, a secondary mechanism is active at higher T that freezes out on cooling.

Next, to study the dynamic nature of the transition of the aliovalently modified ceramic, we measured the temperature dependent permeability at various measurement frequencies. Figures 3.7(a) and (b) show the real and imaginary components of the permeability, respectively. In this figure, both the peaks in μ' and μ'' can be seen to shift to higher temperatures with increasing measurement frequency. For example, the peak in μ' was found to shift from ~135K at 1Hz, to ~155K at 10^3 Hz. These results are unlike that of a normal magnetic phase transition with a long-range spin order parameter. Rather, they clearly demonstrate a dynamic nature to the transition.

Finally, the magnetization behaviors were measured at various temperatures between 5K and 300K, as shown in figure 3.8. The M-H responses all exhibited hysteresis indicating the presence of ferroelectric orders at temperature above the maximum in permeability. This suggests that this phase transition is a magnetic to

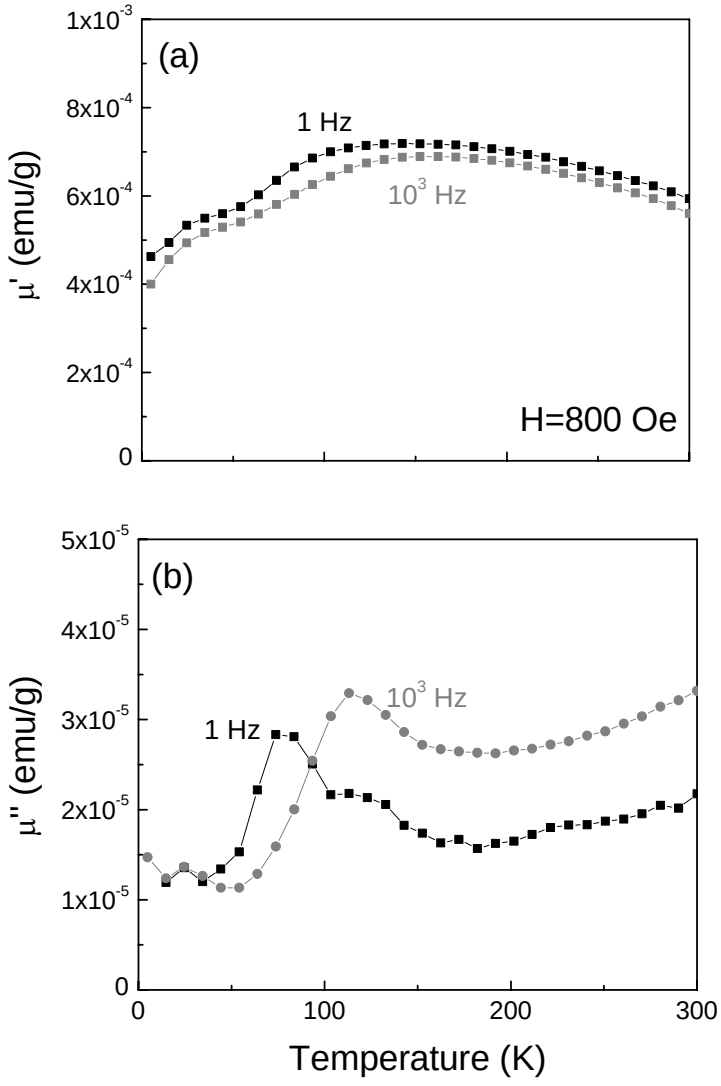

Figure 3.7 Temperature dependent magnetic permeability characteristics of aliovalent-modified BFO-45%PT ceramic at various measurement frequencies demonstrating dispersion (a) real component; and (b) imaginary component.

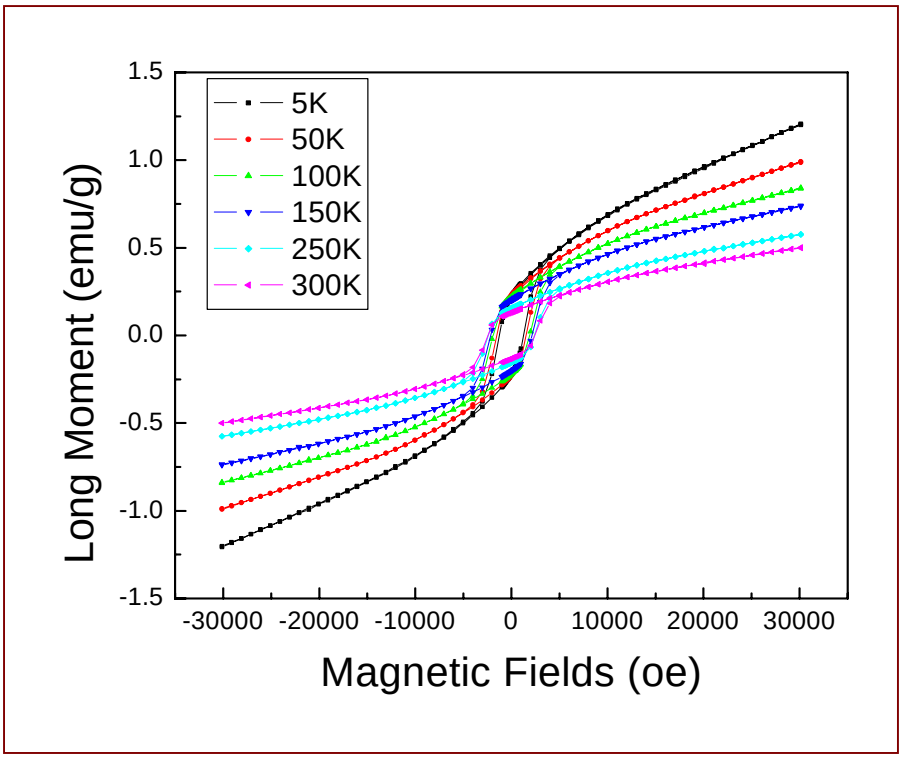

Figure 3.8 Magnetization of modified BLGF-45%PT ceramics as a function of magnetic field H at different temperature.

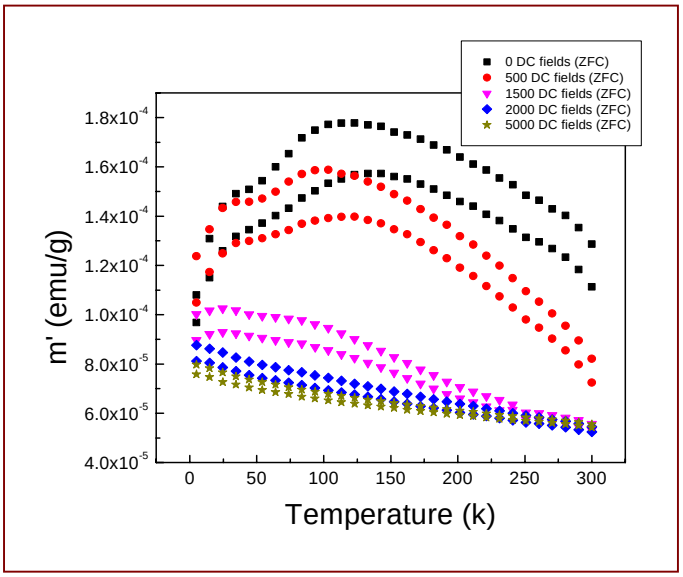

(a)

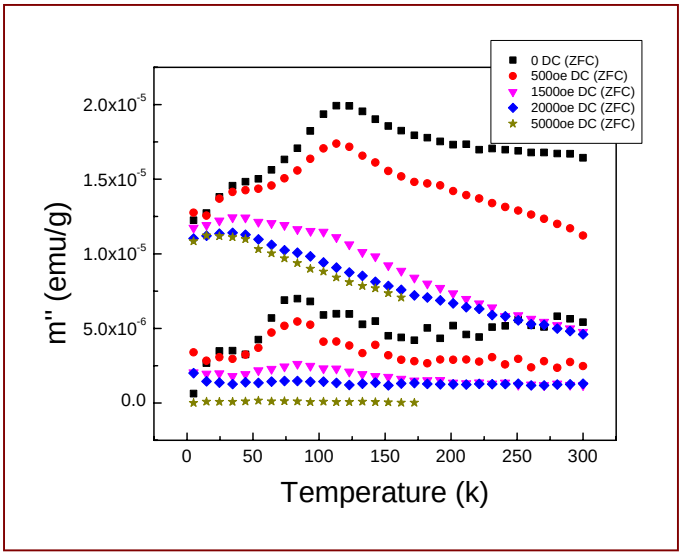

(b)

Figure 3.9 Temperature dependent magnetic permeability characteristics of aliovalent-modified BLGF-45%PT ceramic at DC magnetic fields (a) real component; and (b) imaginary component

magnetic transition. Furthermore, we cooled the ceramic samples with zero magnetic fields. Subsequently, the AC magnetic permeability measurements were performed as a function of temperature at different DC bias. Figures 4.4 (a) and (b) show the real and imaginary parts, respectly. We can see on this figure that the maximum in the permeability was suppressed with increasing DC magnetic bias.

3.3.2 Discussion

We conjecture that aliovalent defects break the translation invariance of the spin cycloid, releasing a latent projection of the antiferromagnetic vector that is trapped within the cycloid. In consideration of the high concentration of aliovalent substitutents, the size of the regions with homogeneous spin order maybe quite small. Their contribution to the magnetic permeability can then be dynamic in nature, where movement and rearrangement of cycloid fragments can give rise to a relaxational response and a significant 'softening' of the permeability. However, this dynamical contribution may freeze out on cooling. In fact, the shift in the temperature of the permeability maximum and of the magnetic absorption peak are quite similar to that previously reported in strongly disordered magnetic systems, such as magnetic spin-glasses [65] and/or systems consisting of superparamagnetic-like clusters [66].

CHAPTER 4 STRUCTURAL STUDIES OF Fe-x%Ga SINGLE CRYSTALS (12<x<25at%) BY NEUTRON DIFFRACTION

In this chapter, we have performed high-resolution neutron and x-ray (XRD) diffraction experiments on (001) oriented Fe-x%Ga crystals for 12<x<25at% at 300K. Both XRD and neutron studies were performed using triple-axis spectrometers. Our experiments reveal (i) a tetragonal splitting along the (002) direction for x=12 and 25at%, but only a single broad averaged-cubic peak for x=20at%; and (ii) a splitting transverse to the (002), revealing a domain texture in which domains are slightly tilted with respect to each other, and whose pattern changes with x.

4.1 Experimental Details

The Fe-x%Ga crystals used in this investigation were grown at Ames Lab by a Bridgman method as previously described [65]. All crystals were then annealed at 1000°C for 168 hours, with heating and cooling rates of 10 degrees per minute, after which the crystals were considered to be in the "furnace-cooled" (or FC) state. The (001)-oriented crystals were then cut into a cubic shape, with dimensions 10*10*2 mm^3 and polished to a 0.25 μm finish. Careful investigations were performed using both x-rays and neutrons, starting from this annealed condition.

The x-ray diffraction (XRD) studies were performed using a Philips MPD high resolution x-ray diffractometer equipped with a two bounce hybrid monochromator and an open 3-circle Eulerian cradle. A Ge (220) cut crystal was used as analyzer, which had a theta-resolution of ~0.0068^{o} (or 0.43 arcseconds). The x-ray wavelength was that of $Cu_{K\alpha}$ (λ=1.5406 Å) and the x-ray generator was operated at 45 kV and 40 mA. The penetration depth in Fe-Ga at this x-ray wavelength is on the order of 3-5 microns. Careful polishing and subsequent annealing were required in order to achieve sharp diffraction peaks. The neutron scattering experiments were performed on the BT9 triple-axis spectrometer located at the NIST Center for Neutron Research. Measurements were made using (i) a fixed incident neutron energy E_i of 14.7 meV; (ii) the (002) reflection of a PG monochromator; and (iii) horizontal beam collimations of 10'-44'-20'-40'. We exploited the PG (002) analyzer to achieve a fine q-resolution, which is needed to detect the subtle broadening and splitting of the Bragg peaks. At 300K, the pseudo-cubic lattice constant of Fe-20%Ga is a_c=2.903Å, correspondingly the reciprocal lattice unit (or l rlu) is $a^*=2\pi/a=2.1632Å^{-1}$. All mesh scans of Fe-x%Ga shown in this study were plotted in reference to this pseudo-cubic reciprocal unit of Fe-20%Ga.

4.2 Results

4.2.1 Fe-12at%Ga

Figure 4.1(a) shows a XRD mesh scan taken about the (002) reflection for Fe-12%Ga. This figure demonstrates the presence of a transverse splitting that is (i) quite

irregular in spacing along (H00); and (ii) quite broad and diffuse. We next determined whether this transverse splitting was identical at various spots across the crystal surface. Figure 4.1(b) shows Ω-line scans taken at 2mm apart from each other. Multiple peaks along the transverse direction can be seen in each case; however, the number of peaks, their relative Ω positions, and relative intensities varied from spot to spot. Because the penetration depth of x-rays is quite small (3-5μm), our results in Figure 4.1 are limited to the outer-layer of the crystal. This outer-layer could be thermally or elastically relaxed: in fact, XRD 2θ line scans of as-grown crystals revealed a tetragonal distortion; whereas on subsequent annealings, a single peak was observed (data not show).

Accordingly, to access the entire volume of the crystal, we measured mesh scans by neutron diffraction. Figure 4.2 shows neutron mesh scans taken around (002) and (200) reflections in the $(H0L)_{cubic}$ zone. Comparisons of the results from the two mesh scans show that the crystal growth direction is not a significant influence. Our mesh scans demonstrate a splitting along the transverse direction, qualitatively similar to that found by XRD. Clearly, the transverse splitting is a bulk phenomenon, and not confined to the outer-layer regions of the crystal. Figure 4.3(a) shows a 2θ line-scan taken along the (002) reflection. A peak splitting can be seen in this figure, indicating two lattice parameters. In an orthogonal coordinate system, this means that the structure has tetragonal symmetry with lattice parameters of a_t=2.887Å and c_t=2.901Å. Figure 4.3(b) shows a line-scan taken along the transverse or Ω direction. A 4-fold splitting can be seen at values of (H00) ≈ -0.027, -0.010, 0.010, and 0.027. We found similar results as those shown in Figure 4.3 for scans taken along the (200) reflection (Figure 4.4).

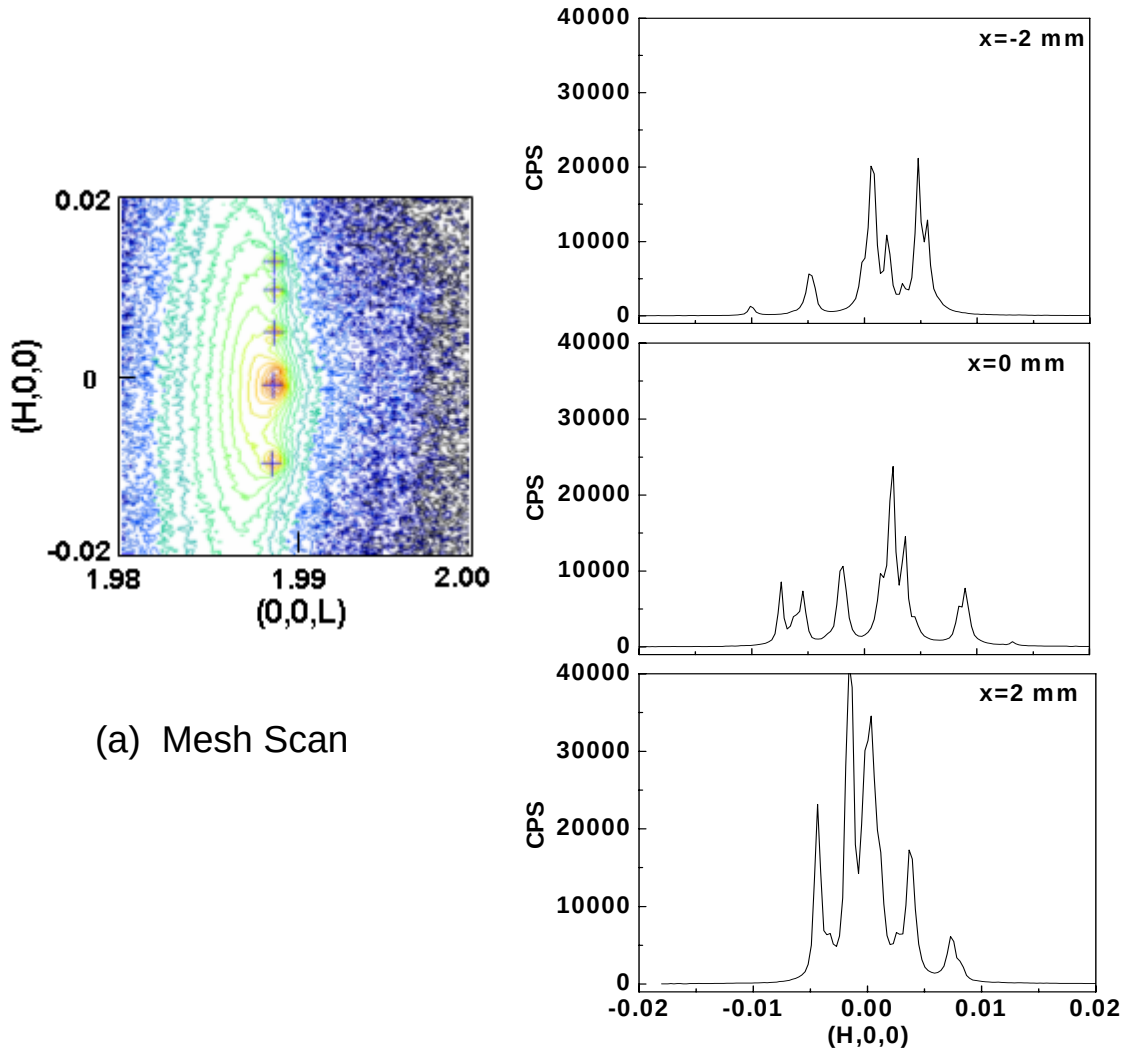

Figure 4.1 XRD data for a (001) oriented Fe-12at%Ga crystal taken along the (002) zone (a) mesh scan; and (b) various Ω line scans taken at different positions along crystal that are 2mm apart.

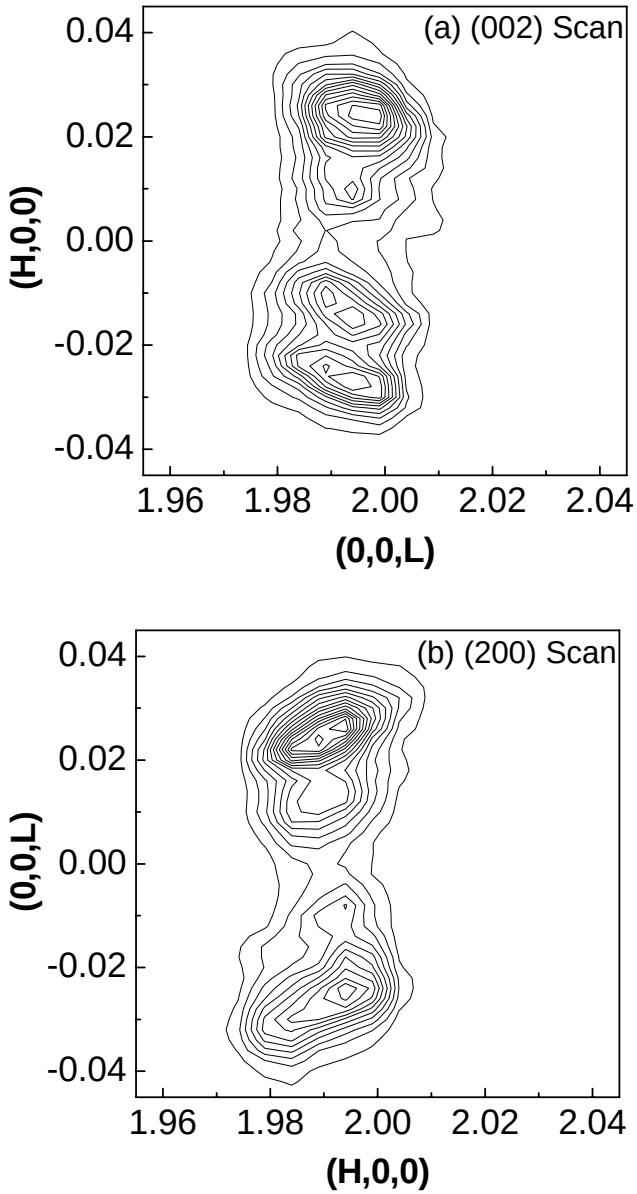

Figure 4.2 Neutron mesh scans for a (001) oriented Fe-12at%Ga crystal taken along (a) the (002) zone; and (b) (200) zone.

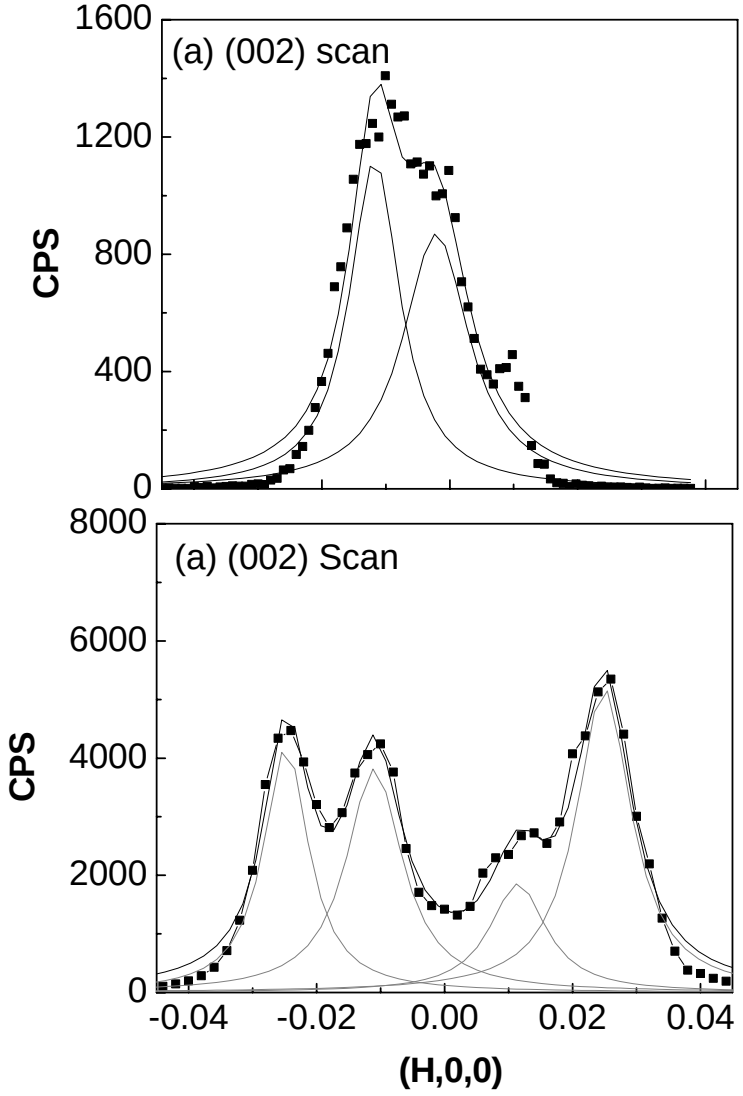

Figure 4.3 Neutron line scans for a (001) oriented Fe-12at%Ga crystal taken along the (002) zone (a) 2θ line scan; and (b) Ω line scan.

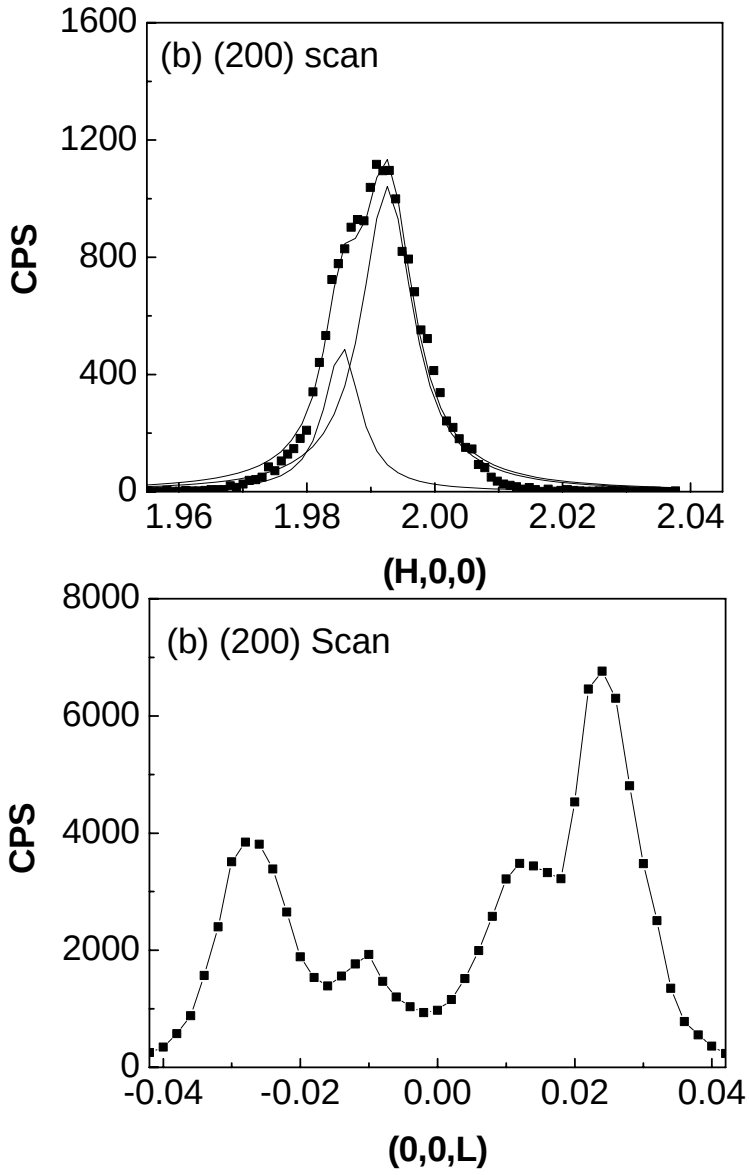

Figure 4.4 Neutron line scans for a (001) oriented Fe-12at%Ga crystal taken along the (200) zone (a) 2θ line scan; and (b) Ω line scan.

The results in Figures 4.2, 4.3 and 4.4 demonstrate that the structure of Fe-12%Ga is tetragonal, and not cubic as previously believed [1,2,6]. Line scans along 2Ω revealed two tetragonal variants with c/a≈1.005. However, the line scans along Ω revealed that there are four sets of such variants. Thus, we conclude that this is not a conventional homogeneous single crystal. Rather, the mesh scans evidence an inhomogeneous crystal that has four-sets of {001} planes that are slightly tilted from each other. Statistically averaged throughout the volume of the crystal (i.e., as determined by neutrons), the axes are separated by $\Omega<0.5^{o}$; however, interrogation of the outer-layer regions (by x-rays) results in pronounced deviation from this averaged value.

4.2.2 Fe-20at%Ga

Figure 4.5 summarizes our neutron investigations of a (001) oriented Fe-20%Ga crystal taken along the (002) reflection. Part (a) of this figure shows a mesh scan. Part (b) shows a 2Ω line scan extracted from the mesh scan. A single broad diffraction peak can be seen in this figure that extends from approximately 1.98≤L≤2.02. Comparisons of this line scan to a corresponding one in Figure 4.3(a) will reveal that the line width of this single peak for Fe-20at%Ga is much broader than the sum of the widths of both peaks for Fe-12at%Ga. Analysis of the peak for Fe-20at%Ga by a single Lorentzian peak resulted in a cubic (C) lattice parameter of a_c=2.903Å. We had also tried fitting with two Lorentzian peaks (not shown), but obtained a fitting with higher error than that obtained by a single peak. Part (c) of Figure 4.5 shows a line-scan taken along the transverse (or Ω)

direction. A broad peak was observed, which consisted of a 3-fold splitting. The Ω-splitting for Fe-20at%Ga was more difficult to resolve than that for Fe-12at%Ga.

The results in Figure 4.5 show that Fe-20at%Ga has a cubic structure with at least 3-sets of {001} planes that are slightly titled with respect to each other. The broad line width along 2Ω suggests a mixture of A2 and DO_3 phases with very fine domain structures. Since the structure of A2 and DO_3 are quite similar, fine-scale precipitation of DO_3 within the A2 matrix would lead to difficulty in distinguishing one phase from another. Thus, we believe that Fe-20at%Ga has an averaged-cubic structure.

4.2.3 Fe-25at%Ga

Figure 4.6 shows our neutron investigations of a (001) oriented Fe-25%Ga crystal taken along the (002) reflection. Part (a) of this figure shows a mesh scan, which reveals a rather sharp peak. Part (b) shows a 2Ω line scan extracted from the mesh scan. A peak splitting can be seen in this figure. The line widths of these peaks are much narrower than for Fe-20%Ga. Analysis of this line scan by two Lorentzian peaks resulted in the tetragonal (T) lattice parameters of a_t=2.914Å and c_t=2.928Å. Part (c) of this figure shows a line-scan taken along the transverse (Ω) direction. A 2-fold splitting with δH≈0.017 can be seen. The results in Figure 4.6 indicate that the DO_3 phase of Fe-25at%Ga has a tetragonal structure with at least 2-sets of {001} planes that are slightly titled from each other.

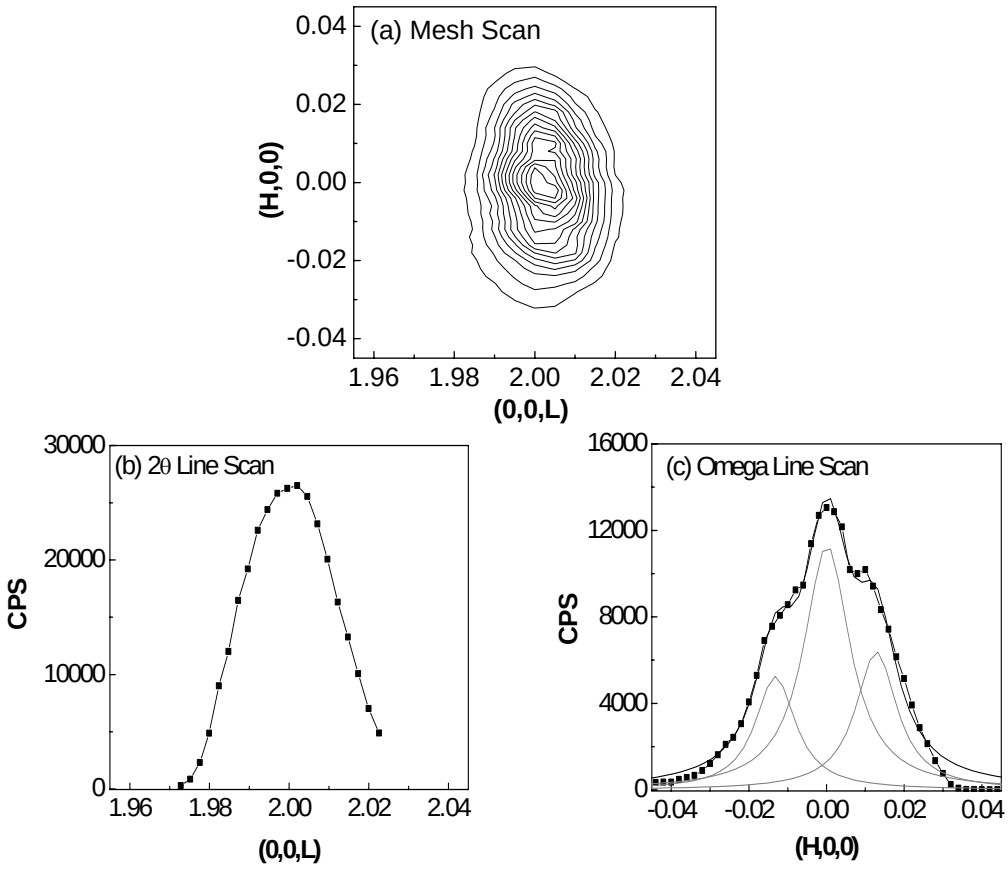

Figure 4.5 Neutron data for a (001) oriented Fe-20at%Ga crystal taken along the (002) zone (a) mesh scan; (b) 2θ line scan; and (c) Ω line scan.

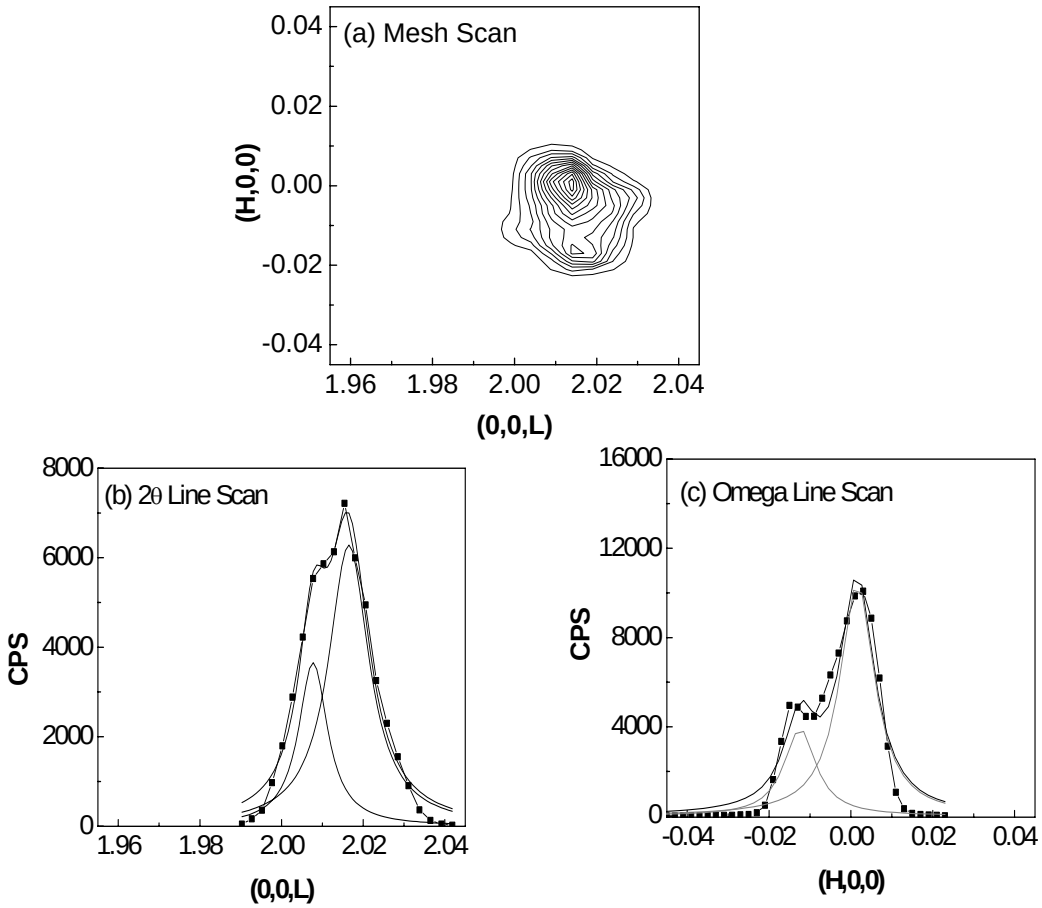

Figure 4.6 Neutron data for a (001) oriented Fe-25at%Ga crystal taken along the (002) zone (a) mesh scan; (b) 2θ line scan; and (c) Ω line scan.

4.3 Discussion

Previous investigations have reported that the A2 phase of Fe-x%Ga is cubic for x<15at%Ga; however, our results demonstrate that it is tetragonal with c/a≅1.005. In addition, we have found that the DO_3 phase has a tetragonal structure, with a similar lattice splitting as A2. Neither phase has a body-center cubic structure; rather both have body-center tetragonal ones. The tetragonal distortions of both structures should be large enough to be readily detected by either high-resolution neutron or x-ray diffraction. However, the tetragonal distortion maybe relaxed at the surface of crystal by either annealing or polishing, making it difficult to detect the distortion by x-rays due to a limit penetration depth.

In the region bridging the A2 and DO_3 phases, an averaged-cubic structure was found. A single diffraction peak was observed along the (002), whose line width was sufficient to mask any possible tetragonal distortion within the A2 or DO_3 phases. Also, the broad peak indicates a very fine domain structure due to the precipitation of DO_3 phases from A2 matrix. Recent results by MFM have shown the presence of miniature magnetic domains, indicative of phase separation by nucleation and growth [14]. Our present and prior [14] results are consistent with (i) a mixed phase region on a fine length scale; (ii) that might be rate-limited by diffusion [1,2,4,5,6].

It should be noted that Fe-12%Ga and Fe-25%Ga crystals (which both possess tetragonal distortion) have much smaller magnetostriction than that of Fe-20%Ga crystal (which possess an averaged-cubic structure). Accordingly, enhanced magnetostriction

can not be entirely attributed to tetragonality and/or Ga pairing. Rather, domain miniaturization may be the main cause of the first peak in the magnetostriction [4]. Miniaturization could significantly enhance the coupling between the magnetization and the lattice, due to enhanced ease of domain rotation/realignment along the easy axis under magnetic fields, i. e., $\lambda_{100} = \delta\varepsilon / \delta H$.

Our results also demonstrate the presence of regions with different c axes that are slightly tilted with respect to each other in both of the T phases, and in the C phase. In each case, the angle of rotation about the transverse direction is quite small ($\Omega<0.5^{o}$). We found that it was possible to distinguish between A2 (x=12at%), intermediate bridging (x=20at%), and DO_3 (x=25at%) phase regions by the type of splitting along the transverse (or Ω) direction. A 4-fold splitting was found for A2 (tetragonal); a 3-fold for the intermediate region (pseudo-cubic); and a 2-fold for DO_3 (tetragonal). The tilting of {001} planes results in a texture pattern that one might loosely say in colloquial-terms resembles a "quilt" – in that it consists of slightly different pieces that have all been stitched together nice and snug, not perfectly, but with some (crystallographic) character. The texture pattern then changes with x, being notable different in the various phase regions of the crystalline solution. We note that changes in texture may accompany corresponding changes in magnetic domain size and regularity [14]: in the A2 phase, macrodomain plates with a strong {001} preferred orientation have been observed by MFM; whereas for DO_3, only miniature domains with much reduced preferred orientation were found.

We do not know whether the inhomogeneity preventing a conventional homogeneous phase is intrinsic, or not. The only thing we can assert with some confidence is that there is no significant difference between {001} directions parallel and perpendicular to the growth direction; and thus, gross fluctuations due to changes in the melt composition during crystal grow are not the cause.

CHAPTER 5 CONCLUSION

Aliovalent modified $BiFeO_3$-based ceramics have been found to have significantly enhanced multiferroic properties, relative to non-substituted $BiFeO_3$ single crystals. Dramatic enhancements in the induced polarization and magnetization have both been found. The observed enhancements are shown to be equal to predicted ones, using a thermodynamic model that includes a magnetoelectric (ME) coupling. The enhancement is caused by the breaking of the translational invariance of a cycloidal spin structure by the random-fields associated with substituents, which couples to the polarization of the ferroelectric phase, via ME exchange.

In addition, aliovalent modification of $BiFeO_3$-based ceramics have been found (i) to result in a significantly enhanced magnetic permeability, relative to non-substituted $BiFeO_3$ single crystals; and (ii) to induce a diffuse magnetic→magnetic phase transition that has superparamagnetic-like characteristics.

Finally, it has been observed that the A2 and DO_3 phases of Fe-x%Ga are both tetragonal. Near the phase boundary between A2 and DO_3, only a single broad diffraction peak was observed that had an averaged-cubic structure. In addition, an unusual splitting along the transverse direction was found, which evidenced that the crystal is inhomogeneous, having multiple {001} planes that are slightly titled with respect to each other.

BIBLIOGRAPHY

1. L. E. Cross, “Ferroic Materials and Composites: Pass, Press, and Future” (1997)

2. Kenji Uchino, Ferroelectric devices, (2000)

3. Ferroelectrics and related materials, Lines and Glass, Oxford (1977)

4. Aizu, K., J. phys. Soc. Jpn. **19**, 918; **20**, 959. Phys. Rev. **140**, 590; **146**, 423

5. Hao Li, Ph.D thesis, University of Maryland, College Park, (2001)

6. Introduction to Solid State Physics, C. Kittel, (1976)

7. Salje, E. K. H. Phase Trasitions in Ferroelastic and Co-elastic Crystals. Cambridge University Press. (1990)

8. V. Muller, A. Fuith, J. Fousek, H. Warhanek and H. Beige, Solid State Communications, 104(8), 455-458, (1997)

9. J. Jian and C. M. Wayman, Materials Letters, Vol. 26, 1-7, (1996)

10. R. E. Newnham, MRS Bulletin, 22(5), 20-34, (1997)

11. Van E. Wood and A. E. Austin, Magnetoelectric interaction phenomena in crystals, edited by A. J. Freeman and H. Schmid, Gordon and Breach Science Publishers, (1975)

12. G. A. Smolenskii and I. E. Chupis, Sov. Phys. Usp. **25,** 475 (1982)

13. Christian Michel, Jean-Michel Moreau, Gary D. Achenbach, Robert Gerson, and W. J. James, Solit State Communications **7**, 701 (1969)

14. J. D. Bucci, B. K. Robertson and W. J. James, J. Appl. Cryst. **5**, 187(1972)

15. F. Kubel and H. Schmid, Acta Cryst. **B46**, 698 (1990).

16. Yu. Ya. Tomashpol’skii, Yu. N. Venevtsev, and G. S. Zhedanov, Soviet Physics-Crystallography **9**, 715(1965)

17. B. Ruette, MS thesis, Virginia Tech (2003).

18. James R. Teague, Robert Gerson and W. J. James, Solid State Communications **8**, 1073(1970)

19. J. Wang, J. Neaton, H. Zheng, V. Nagarajan, S. Ogale, B. Liu, D. Viehland, V. Vaithyanathan, D. Schlom, U. Waghamare, N. Spaldin, K. Rabe, M. Wuttig and R. Ramesh, Science 299, 1719 (2003).

20. I. Sosnowska, T. Peterlin-Neumaier and E. Steichele, J. Phys. C: solid State Phys., **15**, 4835 (1982)

21. I. Sosnowska, M. Loewenhaupt, W. I. F. Davie and R. M. Ibberson, Physica B, 180&181, 117 (1992)

22. A. Zalesskii, A. Zvezdin, A. Frolov, and A. Bush, JETP Letters Vol. 71, 465(2000)

23. A. Zalesskii, A. Frolov, T. A. Khimish, A. Bush, V. S. Pokatilov, A. K. Zvezdin, Europhysics Letters, Vol. 50, 547 (2000)

24. Benjamin Ruette, S. Zvyagin, A. P. Pyatakov, A. Bush, J. F. Li, V. I. Belotelov, A. K. Zvezdin and D. Viehland, Phys. Rev. B **69**, 064114 (2004)

25. Yu.F. Popov, A.M. Kadomtseva, A.K. Zvezdin, et al., in Magnetoelectronic Phenomena in Crystals, Edited by Manfred Fiebig, Kluwer Academic, Boston, (2004)

26. A. M. Kadomtseva, A. K. Zvezdin, Yu. F. Popov, A. P. Pyatakov, and G. P. vorob'ev, JETP Letters **79**, 705(2004)

27. V. V. Sai Sunder, A. Halliyal, and M/ Szymanksi, J. Phys. C 13, 1931 (1980)

28. R. Gerson, P. Chou, and W. J. James, J. Appl. Phys. 38, 55 (1967)

29. R. T. Smith, F. D. Achenbach, R. Gerson, and W. J. James, J. Appl. Phys. 39, 70 (1968)

30. M. Kumer, A. Srinivas, S. V. Suryanarayana, and T. Bhimasankaram, Phys. Status Solid A 165, 317 (1998)

31. Yu. N. Venevstev. G. S. Zhdanov, S. N. Solov'ev, E. V. Bezus, V. V. Invanova, S. A. Fedulov, and A. G. Kapyshev, Sov. Phys. Crystallogr. 5, 594 (1960)

32. S. A. Fedulov, P. B. Ladyzhinskii, I. L. Pyatigorskaya, and Yu. N. Venevstev, Sov. Phys. Solid State 6, 375 (1964)

33. J. R. Cheng, N. Li, and L. E. Cross, J. Appl. Phys., 94, 5153 (2003)

34. J. R. Cheng, L. E. Cross, J. Appl. Phys., 94, 5188 (2003)

35. J. R. Cheng, R. Eitel, and L. E. Cross, J. Am. Ceram. Soc., 86 [12] 2111-2115 (2003)

36. B.D. Cullity, Introduction to Magnetic Materials, Menlo Park, California: Addison-Wesley Publishing Company

37. A. E. Clark, B. F. DeSavage, and E. R. Callen, J. Appl. Phys. **35,** 1028 (1964)

38. K. Hathaway and A. E. Clark, MRS Bull, XVIII, 34 (1993)

39. A.E. Clark, J.B. Restorff, M. Wun-Fogle, T.A. Lograsso, and D. L. Schlagel, IEEE Trans. on Magnetics, vol. 36, p 3238 (2000);

40. A.E. Clark, M. Wun-Fogle, J.B. Restorff, T.A. Lograsso, A.R. Ross, and D. Schlagel, in: H. Borgmann (Ed.), Proceedings of the 7th International Conference on New Actuators, Messe Bremen, Bremen Germany, June 2000, p. 1111.

41. R. C. Hall, J. Appl. Phys. 30, 816 (1960).

42. A. E. Clark, K. B. Hathaway, M. Wun-Fogle, J. B. Restorff, T. A. Lograsso, V. M. Keppens, G. Petculescu and R. A. Taylor, J. Appl. Phys. 93, 8621 (2003)

43. O. Ikeda, R. Kainuma, I. Ohnuma, K. Fukamichi, K. Ishida, J. Alloys and Compounds 1 (2002)

44. T. Lograsso, A. Ross, D. Schlagel, A.E. Clark, and M. Wun-Fogle, J. Alloys and Compounds 350, 95 (2003).

45. N. Kawamiya, K. Adachi, Y. Nakamura, J. Phys. Soc. Jpn. 33, 3318 (1972).

46. T.B. Massalski (Ed.), Binary Alloy Phase Diagrams, 2nd Edition, ASM International, Materials Park, OH, USA, 1990.

47. W. Köster and T. Gödeke, Z. Metallkd. 68, 661, (1977).

48. W. Köster and T. Gödeke, Z. Metallkd. 68, 582, (1977).

49. W. Köster and T. Gödeke, Z. Metallkd. 68, 758, (1977).

50. D. Viehland, J.F. Li, T. Lograsso, A. Ross, and M. Wuttig, Appl. Phys. Lett. 81, 3185 (2002).

51. R. Wu, J. Appl. Phys. 88, 7358 (2002).

52. F. Bai, J.F. Li, D. Viehland, D. Wu, and T.A. Lograsso, (submitted).

53. O. Ikeda, R. Kainuma, I. Ohnuma, K. Fukanichi, K. Ishida, J. Alloy and Compounds 1, 8115 (2002)

54. J.Cheng, W.Zhu, N.Li and L.E.Cross, Fabrication and Characterization of $xBiGaO_3$-$(1-x)PbTiO_3$: A High Temperature Reduced Pb-content Piezoelectric Ceramic, Accepted by Materials Letter.

55. R.E. Eitel, C.A. Randall, T.R. Shrout, S.-E Park Jpn. J. Appl. Phys., Part 1, 41 (2002) 2099.

56. A. Pyatoakov and A.K. Zvezdin (in Press)

57. Yu. F. Popov, A. Zvezdin, G. Vorob'ev, A. Kadomtseva, V. Murashev, and D. Rakov, JETP Lett. 57, 69 (1993)

58. I. Sosnowska and A. Zvezdin, J. Magnetism and Magnetic Materials 140-144, 167 (1995).

59. Yu. F. Popov, A. Kadomtseva, G. Vorob'ev and A. Zvezdin, Ferroelectrics 162, 135 (1994).

60. A. Fedvlov, P.B. Ladyzhinski, I.L. Pyatigorskaya and Y.N. Venevtsev, Soviet Phys.-Solid State, 6 (1964) 375.

61. L.E. Cross, Ferroelectrics 76, 249 (1987).

62. X.H. Dai, Z. Xu and D. Viehland, Phil Mag. B 70, 33-48 (1994).

63. W. Kleemann, Inter. J. Modern Phys. B 7, 2469-2504 (1993).

64. B. Ruette, S. Zvyagin, A.P. Pyatakov, A. Bush, J.F. Li, V.I. Belotelov, A.K. Zvezdin, and D. Viehland, Phys. Rev. B (in Press).

65. K. Binder, A. Young, Rev. Mod. Phys. 58, 4, 801.

66. R. Chantrel, E. Wohlfarth, J. Mag. and Magnetic Mat. 40, 1 (1983).
67. A.E. Clark, M. Wun-Fogle, J.B. Restorff, T. Lograsso, Proc. Fourth Pacific Rim Int. Conf. on Advanced materials and Processing (PRICM4), Eds. S. Hanada, Z. Zhong, S. Nam, R. Wright, (The Japan Institute of Metals), p. 1711 (2001).

VITA

Naigang Wang was born in Changchun, China, on Jan. 12, 1976. He graduated from Jilin University, China, in 1999 with a Bachelor of Materials Science and Engineering. He then enrolled in the Shanghai Institute of Ceramics, Chinese Academy of Sciences and obtained his Master in Material Engineering. In 2002, he entered in the graduate program of Virginia Tech in the Materials Science and Engineering department. He has authored 3 papers. He is a member of the American Ceramic Society.